Novel Dye-sensitized Solar Cell architecture based on microfluidic housing system

Adriano Sacco
I.D. number 169556

Supervisor: Prof. Candido Fabrizio Pirri

Applied Science and Technology Department
Politecnico di Torino

PhD in Electronic Devices
XXV cycle

Non crediamo anche noi uomini che la natura ci parli?

E non ci sembra di cogliere un senso nelle sue voci misteriose,

una risposta, secondo i nostri desideri,

alle affannose domande che le rivolgiamo?

E intanto la natura, nella sua infinita grandezza,

non ha forse il più lontano sentore di noi

e della nostra vana illusione.

(Luigi Pirandello, “Il fu Mattia Pascal”)

Agneddu e sucu e finiu ’u vattiu.

(Sicilian proverb)

Contents

Acknowledgments

I wish to thank all the persons who have supported me during the three years of PhD.

First of all I would like to express my gratitude to Prof. Fabrizio Pirri for having given me the opportunity to work on this fascinating subject, and Prof. Elena Tresso and Dr. Stefano Bianco for the constant guidance thorough the work and for the help they gave me in every moment.

Then I would like to acknowledge the scientific contribution of all the members of the Photovoltaic staff of Politecnico di Torino / IIT@PoliTO: Andrea Lamberti, Diego Pugliese, Nadia Shahzad, Francesca Risplendi, Federico Bella, Rossana Gazia, Angelica Chiodoni, Stefano Bianco, Marzia Quaglio, Giancarlo Cicero, Elena Tresso. Among them, a special thank goes to my "twin" Andrea, who shared with me all the work done during these three years.

I would like to thank all those persons who helped out with measurements: Dr. Marco Armandi, Dr. Micaela Castellino, Dr. Diego Manfredi and Dr. Alessandro Virga.

I also thank Prof. Anca Ionescu, Dr. Simelys Hernandez, Dr. Federica Cappelluti and Miss Shuai Ma for their scientific contribution.

I would like to gratefully acknowledge Daniele Flore, Lidia Rolle, Irene Berardone and Matteo Gerosa for their exceptional scientific contributions in the framework of their diploma works, which considerably enriched the output of this work. All the partners involved in the framework of different collaborations are acknowledged for their help, especially Dr. Pino Caputo, Dr. Giorgia Musso and Dr. Claudia Barolo for the synthesis of the organic dyes studied in this work.

I thank the whole "Materials and Processes for Micro & Nano Technologies" group of Politecnico di Torino for the great support. Among them, a special thank to my colleagues (and friends!!!) Micaela and Alessandro, and to Francesca and Serena for the funny lunchtimes. I also thank the Microla Optoelectronic staff for the wonderful working atmosphere.

Moreover I would like to thank all the people working at the Center for Space Human Robotics of Istituto Italiano di Tecnologia for the stimulating and exciting working atmosphere. A special thank goes to Andrea, Valentina, Stefano, Giancarlo, Nadia and Annalisa for the friendly relax moments.

Dulcis in fundo, a special thank to Rossana, who always supported me, and to my family and friends in Palermo for their love and support all through the different stages of my life.

List of abbreviations and symbols

β	constant phase element index
β_{CE}	constant phase element index associated to counter electrode double layer capacitance
δ	electrolyte diffusion layer
η_{coll}	charge collection efficiency
η_{inj}	charge injection efficiency
η_{lh}	light harvesting efficiency
η_{reg}	regeneration efficiency
γ	effective recombination order
λ	wavelength
ω	angular frequency
ω_d	characteristic frequency of diffusion in the electrolyte
ω_n	rate constant for recombination
ω_t	characteristic frequency of diffusion in the oxide
$\Phi(\lambda)$	incident photon flux
$\phi(\lambda)$	incident light power density
ρ	constant accounting for the dependance of recombination resistance on the applied voltage
σ	constant accounting for the dependance of chemical capacitance on the applied voltage
τ_{CE}	counter electrode charge transfer time
τ_n	electron lifetime
τ_{pc}	time constant for photocurrent response
τ_t	electron transport time

φ elevation angle

a absorbance

A cell area

AC Alternating Current

ACN acetonitrile

AM Air Mass

BET Brunauer-Emmett-Teller

BIPV Building-Integrated PhotoVoltaics

c speed of light

C concentration of absorbing species

c_μ distributed chemical capacitance

C_0 chemical capacitance value at 0 V bias

C_μ total chemical capacitance

$C_{I_3^-}$ steady state bulk concentration of I_3^-

C_{CE} counter electrode double layer capacitance

C_{CO} transparent conductive oxide contact capacitance

C_{TCO} transparent conductive oxide double layer capacitance

CA Contact Angle

CB Conduction Band

CDCA chenodeoxycholic acid

CPE Constant Phase Element

d photoanode film thickness

D_0 diffusion coefficient of conduction band electrons

$D_{I_3^-}$ diffusion coefficient of I_3^-

D_{n} chemical diffusion coefficient

DI deionized

DFT Density Functional Theory

DSC Dye-sensitized Solar Cell

$E(\lambda)$ solar spectral irradiance

E_C conduction band energy

EQE External Quantum Efficiency

EtOH ethanol

FESEM Field Emission Scanning Electron Microscopy

FF Fill Factor

FTO fluorine-doped tin oxide

GuSCN guanidinium thiocyanate

h Planck constant

HOMO Highest Occupied Molecular Orbital

i_0 diode dark current

i_{ph} diode model photocurrent

I_{max} current at maximum power point

I_{sc} short circuit current

IMPS Intensity Modulated Photocurrent Spectroscopy

IMVS Intensity Modulated Voltage Spectroscopy

IPCE Incident Photon-to-electron Conversion Efficiency

IQE Internal Quantum Efficiency

IR infrared

ITO indium tin oxide

I-V Current-Voltage

j imaginary unit

J_{sc} short circuit current density

k absorption coefficient

k_B Boltzmann constant

k_d rate constant for decay of the excited dye

k_{inj} rate constant for electron injection

k_{rec} rate constant for electron-oxidized dye recombination

k_{reg} rate constant for regeneration

L_n diffusion length

LDPE low-density polyethylene

LUMO Lowest Unoccupied Molecular Orbital

m diode ideality factor

MPN 3-methoxypropionitrile

MT Multiple Trapping model

n_0 concentration of conduction band electrons in the dark

n_C concentration of conduction band electrons

n_T concentrations of trapped electrons

N number of electrons transferred in the counter electrode reaction

NP nanoparticle

NT nanotube

OCVD Open Circuit Voltage Decay

P_{inc} incident optical power

P_{max} maximum power

PCE photoconversion efficiency

PDMS polydimethylsiloxane

PMMA poly(methyl methacrylate)

q elementary charge value

Q constant phase element prefactor

q_μ distributed constant phase element associated to chemical capacitance

Q_μ total constant phase element associated to chemical capacitance

Q_{CE} constant phase element associated to counter electrode double layer capacitance

QE Quantum Efficiency

$R(\lambda)$	reflectivity of cell surface
r_{ct}	distributed electron recombination resistance
r_t	distributed electron transport resistance
R_0	electron recombination resistance value at 0 V bias
R_{CE}	counter electrode charge transfer resistance
R_{CO}	transparent conductive oxide contact resistance
R_{ct}	total electron recombination resistance
R_d	electrolyte diffusion resistance
R_s	cell series resistance
R_S	transparent conductive oxide series resistance
R_{sh}	cell parallel resistance
R_t	total electron transport resistance
R_{TCO}	transparent conductive oxide recombination resistance
RF	radio-frequency
s	scattering coefficient
S	sensitizer ground state
S^*	sensitizer excited state
S^+	sensitizer oxidized state
SMU	Source Measure Unit
SSA	Specific Surface Area
T	absolute temperature
T_m	melting temperature
TBA	tetra-n-butylammonium
TBP	4-tert-butylpyridine
TCO	transparent conductive oxide
TDDFT	Time Dependent Density Functional Theory
TLM	Transmission Line Model

UV	ultraviolet
V_{max}	voltage at maximum power point
V_{oc}	open circuit voltage
V_{th}	thermal voltage
W_{inc}	incident optical power density
W_p	Watt-peak
XRD	X-Ray Diffraction
Z_{CE}	counter electrode impedance
Z_d	electrolyte diffusion impedance
Z_G	Gerisher impedance
Z_{ph}	photoanode impedance

Chapter 1

Introduction

One of the main problem humanity will have to deal with during the next years is the energy production. The world population exceeded 7 billion at the end of 2011 and consumes a quantity of energy estimated in $5.6 \cdot 10^{20}$ J per year, that corresponds to a continuos demand of 17.8 TW. As the world population is increasing and the society is becoming more advanced in technology and economy, more energy is being consumed to keep up with the development, and the demand on energy boomed over the past years. Presently the annual world primary energy consumption increases by 1.6% per year and is estimated to be about to $8.1 \cdot 10^{20}$ J by the year 2035 (that means 25.8 TW) [1].

At the moment, the energy economy is still highly dependent on three forms of fossil fuels (oil, natural gases and coal) that cover more than 85% of the total energy production. However, the world will shortly come to an end of fossil fuels as the primary energy resource. In fact, at current reserves-to-production ratio, oil might run out in around 40 years, natural gases can last for about 60 years and coal, being the most abundant, for 150 years [1]. Moreover different economic reasons (periodic increases of oil price, interruption in gases distribution, politic troubles in the Middle East region) lead to continuos increase of the fossil energy cost. Finally, we have to keep in mind the impact of energy production from fossil fuels on the environment. In fact the global concentration of carbon dioxide, the most important greenhouse gas, has increased markedly as a result of human activities, primarily due to fossil fuel use. The raise in CO_2 concentration led to an increase of the average global temperature, a phenomenon known as "global warming". Averaged over time, the rate of temperature increase has doubled over the last 50 years compared to that of the last 100 years, and in total, the average global temperature raised by 0.76 ºC since the beginning of the twentieth century. It has been predicted that the average global temperature will increase between 0.6 and 4.0 ºC in the coming 100 years, depending on model parameters such as world population growth, primary energy source, and economic growth [2]. In the long-term, this

could influence the climate zones and disturb well-established ecological systems. Eventually, if the temperature continues to increase, this will influence our everyday lives, since it changes the conditions of, for example, agriculture and fishing. So, the huge increase in worldwide energy consumption, along with the threat that fossil energy resources might soon draw to an end, the concerns about impending energy crises and the climatic consequences of the worldwide CO_2 production, raised new interest in alternative energy sources on a political and economical level during the last years. For example, in 2008 the EU decided that no later than 2020 the carbon dioxide emissions should decrease by 20% and the 20% of the energy produced in EU should originate from renewable energy sources [3].

To be economically competitive, alternative energy sources have to be efficient, inexpensive and environmentally friendly, i.e. they have to be sustainable. For example, nuclear power is an alternative energy source that cannot be defined sustainable because its generation lead to the production of radioactive wastes, that are very difficult to dump. During recent years, particular attention has been devoted to renewable energy sources, which are inexhaustible on human life timescale and whose use does not affect the environment (they are defined "green" energy). At present, hydroelectricity and wind power represent two of the most widely used forms of renewable energy sources. The first is based on the production of electrical power through the use of the gravitational force of falling water, the second one is based on the conversion of wind kinetic energy into other forms of energy, like electricity or mechanical power. However hydropower presents some environmental problems related to the impact of artificial basins and both sources need the fabrication of infrastructures for the bulk transfer of electrical energy, because usually the production sites are very far from the end user sites. Geothermal plants exploit the thermal energy that is stored under the earth's crust; they can work 24 hours per day and are not dependent on climatic conditions, but, due to the fact that the thermal energy is scarcely transportable, its use is limited to the regions close to the plants. Biomass is another important form of renewable energy source: usually it is plant matter used to generate electricity (through the use of steam turbines) or to produce heat (for example by direct combustion). There are also some minor renewable energy sources related to sea and ocean waters, like tidal and wave power. Finally there is the energy coming from the sun. Solar energy can be exploited to generate heat or electricity. In the first case the conversion is obtained through solar thermal collectors, in which the sun light is used to heat a liquid that subsequently transfers the energy to water contained in a reservoir. These collectors are mainly used for heating water or air for residential and commercial use. In the second case, the solar panels generate directly electricity exploiting the photoelectric effect, as explained in details in the next sections.

1.1 Photovoltaics

Light coming from the sun represents a huge reservoir of clean energy; its use, by means of photovoltaic technologies, could help reducing CO_2 emissions. The photovoltaics possess the great advantage of local energy generation, which is the production of energy by means of domestic

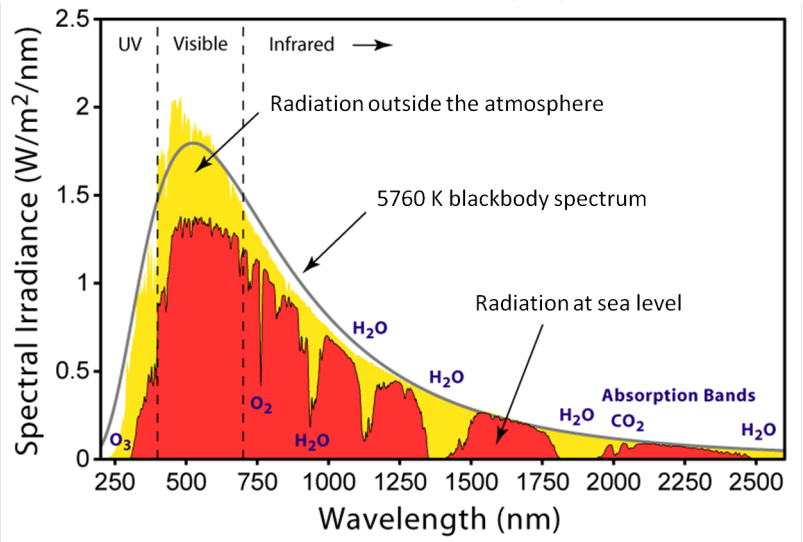

Figure 1.1: Solar radiation spectrum (adapted from [5]).

implants distributed all over the earth's surface, especially in rural or quasi-deserted areas (off-grid operation), avoiding losses related with energy transportation. Moreover photovoltaic devices have other competitive advantages such as little need for maintenance and silence, which are ideal for usage in mobile applications. The potential of using the sun as a primary energy source is enormous. One simple reason is that the earth receives $3 \cdot 10^{24}$ J of energy per year from the sun (about 10000 times the actual global energy consumption); this means that covering only 0.1% of the earth's surface area (corresponding to 1% of desert areas) with solar cells of 10% efficiency would satisfy our present needs [4]. The sun emission wavelength range covers the ultraviolet (UV), visible and infrared (IR) regions of electromagnetic spectrum, with a maximum peak around 500 nm. Its spectrum is similar to that of a blackbody at 5760 K and it is influenced by the absorption of some molecules present in the atmosphere, such as O_3, CO_2, H_2O (see Fig. 1.1).

However the earth's surface is not uniformly irradiated. This non homogeneity depends on different factors: clouds (that absorb a high amount of radiation), angle of incidence of sunrays (the higher is the tilt of sunrays, the lower is the energy that arrives to the soil) and atmospheric mass. The maximum intensity of solar irradiation occurs when sun is at the zenith (90° with respect to the horizon), that corresponds to the shortest path that sunlight covers through the atmosphere. This distance is defined as Air Mass (AM), which is an index expressed through the formula:

$$AM = \frac{1}{\cos \varphi} \tag{1.1}$$

where φ is the elevation angle (see Fig. 1.2). This concept permits to quantify the output power density (defined as *irradiance*) as a function of sun position. AM0 conditions are related to irradiance outside earth's atmosphere, where power density is called *solar constant* (about 1360 W/m^2). In order to compare measurements and efficiencies of different solar cells under the same protocol, standard conditions have been defined (IEC 61215, IEC 61646, UL 1703 [6]). The so-called Watt-peak (W_p) corresponds to the power generated by the solar cell illuminated with a light intensity

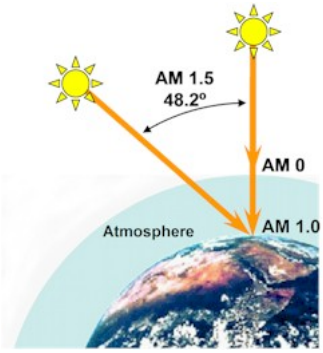

Figure 1.2: Air Mass (AM) definition [8].

equal to 1000 W/m^2, under AM1.5 conditions (elevation angle equal to 48.2°, corresponding to United States, Europe and Japan latitudes) and with a temperature of 25 °C. Finally it is important to distinguish between two different sunlight components, which are the direct and the diffuse light. The first is the light that hits directly the earth's surface, while the second derives from the scattering through the atmosphere; this part represents about the 15% of total sunlight [7]. Usually measurements under simulated sunlight (using solar simulators) are performed under AM1.5G irradiation, where *G* stands for Global, that is the sum of direct and diffuse light.

1.2 Solar harvesters

Solar cells are the base elements of the photovoltaic harvesting, being the fundamental components of solar panels. Upon absorption of sunlight, they can generate electricity using the photoelectric effect.

In Fig. 1.3 the typical current-voltage (I-V) characteristic of a generic solar cell is presented together with some important figures of merit: the open circuit voltage V_{oc} (the maximum voltage when no current flows through the cell), the short circuit current I_{sc} (the maximum current when the cell electrodes are short-circuited) and the maximum power point P_{max} (the point in which the current $\times$voltage product is maximum ($P_{max} = I_{max} \cdot V_{max}$)). It is worthy to note that in the field of photovoltaics instead of short circuit current and maximum current is preferable to refer to short circuit current density J_{sc} and maximum current density J_{max}, simply dividing the currents for the cell area *A*. Another important feature derived from I-V measurement is the fill factor FF, which is a measure of the cell quality. The fill factor is defined as

$$FF = \frac{J_{max} V_{max}}{J_{sc} V_{oc}} \tag{1.2}$$

The higher is FF, the higher is cell quality (ideal cell would have FF equal to 1). Finally the most important parameters obtainable from I-V measurement is the photoconversion efficiency (PCE), defined as the ratio between the electrical power produced by the cell and the optical power impinging on the cell itself P_{inc}:

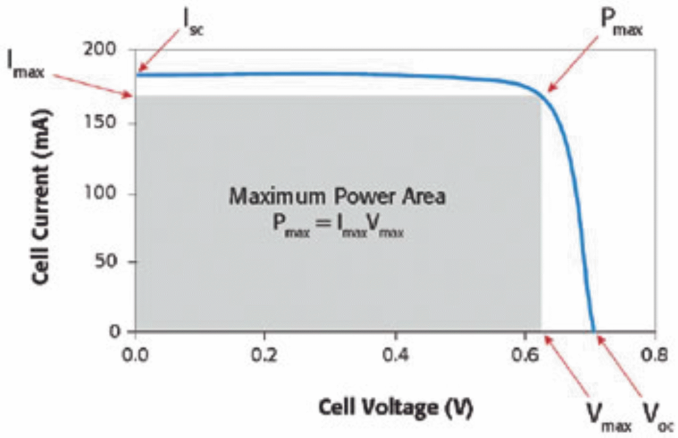

Figure 1.3: Typical I-V characteristic of a solar cell [9].

$$PCE = \frac{P_{max}}{P_{inc}} = \frac{J_{sc}V_{oc}FF}{W_{inc}} \tag{1.3}$$

where W_{inc} is the optical incident power density (equal to 100 mW/cm^2, also called 1 *sun*, under standard AM1.5G condition).

In Fig. 1.4 the typical quantum efficiency (QE) of a solar cell is depicted. The QE represents the number of electrons that are produced by an impinging photon for a given wavelength λ. For a solar cell two different QEs can be defined, the internal quantum efficiency (IQE) and the external quantum efficiency (EQE), that differ in terms of reflected light: all impinging photons are considered in the calculation of EQE, while IQE accounts only for photons that are not reflected by the cell surface: $EQE(\lambda) = [1 - R(\lambda)] \cdot IQE(\lambda)$, with $R(\lambda)$ reflectivity of the surface. Quantum efficiency is a crucial parameter for a solar cell that determines the maximum current obtainable from the device; in fact it depends on the light harvesting efficiency η_{lh}, the charge injection efficiency η_{inj} and the charge collection efficiency η_{coll}. Using the external quantum efficiency (also known as Incident Photon-to-electron Conversion Efficiency, IPCE) definition, the short circuit current density J_{sc} can be expressed as:

$$J_{sc} = q \int \Phi(\lambda) IPCE(\lambda) d\lambda \tag{1.4}$$

where q is the elementary charge value, $\Phi(\lambda) = E(\lambda)/(hc/\lambda)$ is the incident photon flux for a given wavelengh λ, $E(\lambda)$ is the solar spectral irradiance, h is the Planck constant and c is the speed of light.

1.2.1 Solar cell technologies

Currently the photovoltaic market (for terrestrial applications) is dominated by mono- and poly-crystalline bulk silicon, which offer the best compromise between costs and performances (about 1.2 €/W$_{\text{p}}$ with efficiencies as high as 20%). Nevertheless under diffuse radiation, amorphous thin films, nanostructured materials and polymers can absorb a higher amount of incoming light with

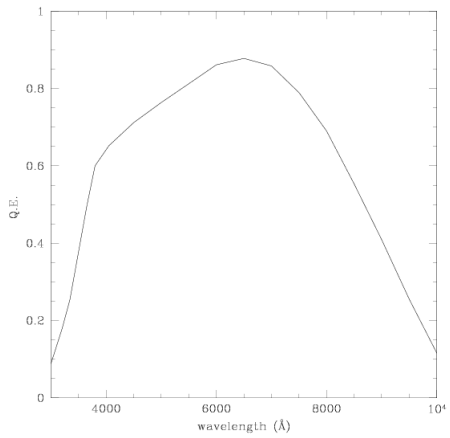

Figure 1.4: Typical quantum efficiency of a (silicon) solar cell [11].

respect to crystalline materials. For this reason the interest on the so called ‘‘second and third generation’’ solar cells is going to increase, thanks to the chance of usage under both direct and non-direct radiation conditions. The ‘‘second generation’’ solar cells are made by thin films of amorphous materials (e.g. silicon, cadmium telluride, copper indium gallium selenide), while the dye-sensitized solar cells (fabricated using a nanostructured semiconductor layer) or the organic solar cells (made with polymers) are acknowledged as the ‘‘third generation’’ or ‘‘emerging concepts’’ in photovoltaics [10].

First generation solar cells are the so-called *solid junction cells*, in which the constituent material is the silicon (both in mono- and poly-crystalline forms). Historically, they are the “older” devices, being firstly fabricated in 1954 [12]. Si energy gap is about 1.1 eV, so it absorbs solar radiation in the visible and near IR wavelength range (up to 1100 nm). The Si cell fabrication technology is based on the formation of a *p-n* junction by means of doping elements (like boron or phosphorus). When the two types of semiconducting material are in close contact, a discontinuity of the Fermi level is created at the interface, thus allowing the charge diffusion into the two materials (holes, that are present in the p material due to the presence of doping species, diffuse in the n material, and vice versa). In this way the concentration gradient present at the interface generates an electric field in the so-called *depletion region*, which limits and finally stops the flux of charges, thus creating a potential difference known as *built-in potential*. When the device is illuminated, photons with energy higher then Si bandgap are absorbed, thus creating hole-electron couples. If the material has a high degree of crystallinity, the minority carriers (holes in the n region and p in the n region) are driven to opposite sides of the junction by the built-in voltage leading to current flow in the external circuit [13]. The industrial production allows obtaining wafers with a thickness of about 0.2 mm for the monocrystalline silicon and 0.3 mm for the polycrystalline one; the Si monocrystals are of electronic grade purity, while this grade is lower for the polycrystalline Si. Thanks to this elevated purity, mono-Si cells present laboratory efficiency values as high as 25% (20% for the poly-Si), but they are quite expensive and with a long *payback time* (the payback time is the time interval in which a cell produces the amount of electricity necessary to cover the

energy spent during its fabrication); for monocrystalline silicon this value is 4 years [14].

Photovoltaic cells belonging to the second generation are known as *thin film solar cells*, because their constituent material thicknesses are about 100 times lower with respect to first generation devices (typical values are in the range of few μm). This is due to the fact that the used materials have an absorption coefficient higher than the Si one. Like the first generation devices, also the thin film cells are based on p-n junction, but, since the thickness is extremely lower, the costs of raw materials and the production technologies are cheaper, being about 0.7 €/W_p; as a consequence their payback time is lower. Moreover an attractive feature for these cells is that they can be deposited on flexible and partially transparent substrates. Among the used materials, the most affirmed technology is that of amorphous silicon (a-Si), which is often used in the so-called double- or triple-junction cells: these devices are fabricated superimposing various cells based on materials with different bandgap (obtained by tuning the concentrations of the amorphous silicon-based alloys or the microcrystal fraction), that absorb in distinct wavelength regions [15]. Other used materials are: cadmium telluride (CdTe), whose photovoltaic performances are quite similar to crystalline Si, but with the advantages of diffuse light absorption and immunity to increasing temperature issues [16]; copper indium selenide ($CuInSe_2$, CIS), that presents high long-term stability and interesting application as *building-integrated photovoltaics* (BIPV, that are photovoltaic materials used to replace conventional building materials) [16]; copper indium gallium (di)selenide ($CuInGaSe_2$, CIGS), that have the highest efficiency (up to 19%) between the thin film solar cells [15]. All the materials used in the second generation photovoltaics, with the exception of a-Si, are highly toxic and polluting and consequently there are some problems related to their use, especially for the post-consumer waste. Concerning the amorphous silicon, it is characterized by a reduced stability over time [16].

The third generation photovoltaics groups all the solar cells whose principle of operation is different from the classical p-n junction. These devices can, in principle, overcome the so-called *Shockley-Queisser limit*, which is the maximum theoretical efficiency of a solar harvester based on the p-n junction. This limit was calculated by Shockley and Queisser in 1961 [17] and it is around 33.7% for a p-n junction with a band gap of 1.4 eV under 1 sun illumination (for Si-based devices it is below 30%). According to their study, the remaining energy coming from the sun is lost due to three different reasons:

- not the entire solar spectrum has the energy required by an electron to overcome the energy gap;
- a part of energy is lost when hot photogenerated electrons and holes relax to the band edges;
- the third part is not related to the solar spectrum but to the tradeoff between low radiative recombination versus high operating voltage caused by different values of electron and hole mobility.

Designs that exceed the Shockley-Queisser limit work by overcoming one or more of these three loss processes, for example by modifying the material band gap, by reducing the thermal dissipation or by concentrating the solar radiation. Between all the third generation devices, the most

promising ones are the organic cells and the dye-sensitized solar cells. The former are based on conducting polymers, and their standard architecture were firstly proposed by Sariciftci and co-workers [18]. These cells are constituted by an anode (usually a glass covered with a *transparent conductive oxide*, TCO) and a metallic cathode, separated by a *polymer blend*, which is a heterogeneous mixture of two immiscible polymers: one is defined as *donor* (usually is the poly(3-hexylthiophene), P3HT) and the other is the *acceptor* (usually the Phenyl-C61-butyric acid methyl ester, PCBM, that is a Fullerene derivative). The exciton generation occurs in the donor material and the subsequent charge separation at the donor/acceptor interface. Numerous are the advantages of these devices, like low material cost, easy and low-cost fabrication process, flexibility; on the other hand, the issues are the poor efficiency and low long-term stability. Dye-sensitized solar cells (DSCs) are photoelectrochemical devices in which the light is absorbed by dye molecules that generate electrons and transfer them to a porous semiconductor (TiO_2 nanoparticle in the standard configuration) deposited on a TCO-covered glass, whic acts as a *photoanode*; the *counter electrode* is a TCO-covered glass on which a thin film of Pt is deposited; the regeneration of dye molecules is obtained through a hole conducting material (usually a redox couple dissolved in an organic solvent). The first DSC was fabricated in 1991 by O'Regan and Grätzel [19], so from the name of one of their inventor they are known as Grätzel's cells. These devices are characterized by an efficiency of about 10% [20] and low fabrication costs (the goal is to achieve 0.3 €/W_p, with a payback time of 1 year), and have some peculiar features like the transparency and the possibility of been fabricated in different colors (thanks to the usage of different dyes), thus being interesting as BIPV. The major drawback lays in a limited stability over time, mainly due to the presence of the liquid electrolyte, whose evaporation and/or leakage is still an unsolved issue (even if different attempts have been made in order to reduce these phenomena, like sealing the devices with thermoplastic hot melt glue and some resins). A detailed description of the working principle of this kind of cell will be presented in Chapter 2.

In Fig. 1.5 the best cell efficiencies for the different kind of solar devices are reported. It can be seen that for first generation devices (represented as blue points in the graph) the state-of-the-art efficiency was reached almost ten years ago, while research on second and third generations (green and orange points, respectively) is currently in progress, thus demonstrating the interest in finding some possible low-cost competitor to Si-based solar cells.

1.3 Aim of the work

As described in Section 1.2.1, in the standard configuration DSCs are sealed with a thermoplastic material in order to prevent some problems related to the liquid electrolyte leakage and evaporation, and to the inlet of air and water vapor that can degrade dye molecules. Nevertheless in various research laboratories all over the world, for quick tests on different constituent materials (semiconductor, dye molecules, etc...), the cell assembly can be obtained by simply sandwiching the two electrodes using standard clips: this type of closure cannot obviously avoid the electrolyte leakage. Moreover in this way the distance between the electrodes is not a fixed parameter, giving birth to problems related to cell fabrication reproducibility.

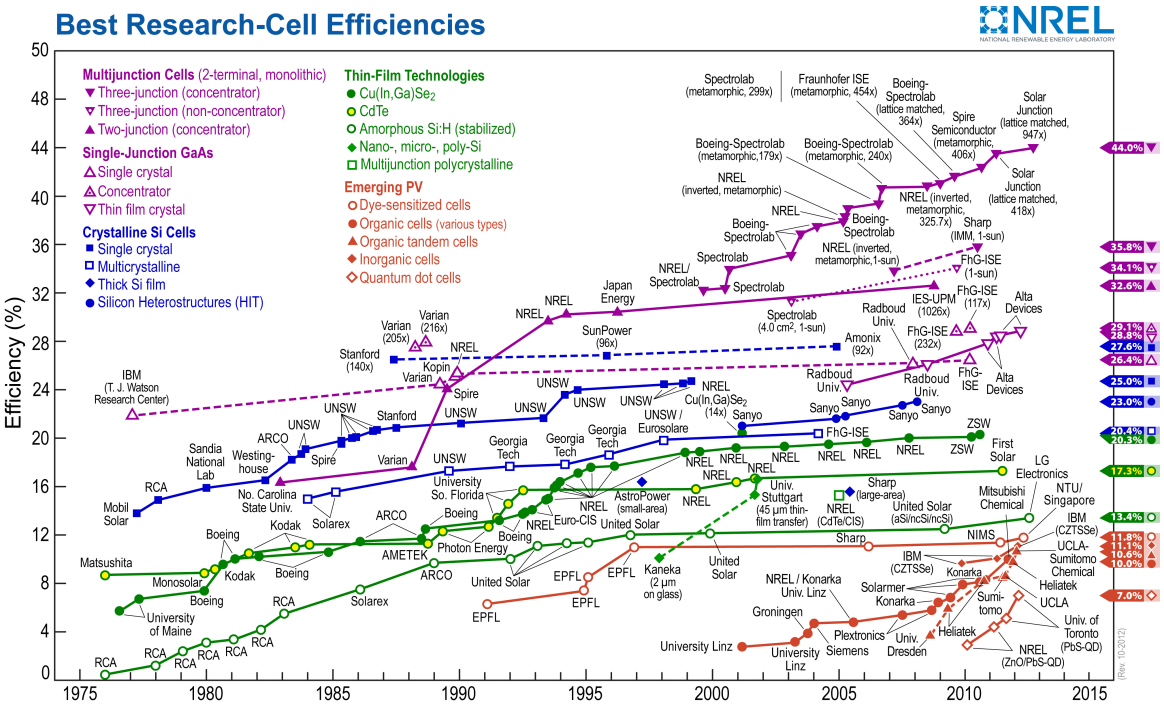

Figure 1.5: Best research-cell efficiencies chart [21].

The present work is focused on the design, fabrication and characterization of a novel dye-sensitized solar cell architecture exploiting some microfluidic concepts. By using this innovative approach, it became possible to fabricate small laboratory test-cells with a high degree of assembly reproducibility, and develop some interesting applications, like the analysis of the cell components over time, without compromising the cell integrity. The proposed architecture has been used in the experimental test of some innovative materials. The study is of experimental nature and supported by different photoelectrochemical analytical techniques, in order to study the cell behavior.

The thesis is then subdivided into four main parts: Chapters 2 and 3 present a detailed description of DSC structure, components and working principle, and experimental techniques exploited for device characterization; Chapter 4 is devoted to the description of materials and instrumentations used thorough the work, together with the device fabrication procedures; Chapters 5 and 6 discuss the results of the experimental work, in particular about the microfluidic device characterization, and the use of the novel architecture in the test of different innovative materials; finally Chapter 7 presents the general conclusions on the basis of all previous sections, together with a brief discussion of future work to be done.

Almost all the experiments and characterizations were performed at the Center for Space Human Robotics @ PoliTO of the Istituto Italiano di Tecnologia (IIT) in Torino. The optical and morphological characterizations were carried out at the Applied Science and Technology Department (DISAT) of the Politecnico di Torino, in Torino. The fluidic tests were conducted in the Material and Microsystems Laboratory (χ-lab) of the Politecnico di Torino, in Chivasso.

Chapter 2

Dye-sensitized Solar Cells

This chapter is fully dedicated to the description of dye-sensitized solar cells. As already mentioned in Section 1.2.1, these devices belong to third generation photovoltaic cells, characterized by low-cost materials and fabrication processes, thus being an interesting alternative to the more expensive Si-based solar cells. Firstly a detailed description of DSC architecture and components will be presented. Then the cell operating principle will be explained, and particular care will be devoted to the charge transfer processes occurring inside the device.

2.1 DSC structure and components

The standard architecture of a DSC, reported in Fig. 2.1, is made up of a photoanode, a counter electrode and a liquid electrolyte solution [22]. The photoanode substrate is constituted by a glass slice covered by a thin transparent conductive oxide (TCO) film. A porous wide band gap semiconductor is deposited onto TCO, and this film is covered with a monolayer of dye molecules, that are anchored on its surface. The photoanode is said to be "sensitized" by these molecules, for this reason the dye is also called *sensitizer*; dye molecules are responsible for light absorption and photoelectron generation. Since the optical cross section of a dye molecule is much lower with respect to the surface it occupies, a great number of molecules is needed in order to achieve a relatively high light absorption. For this reason a nanostructured layer with a high *specific surface area* (SSA) is used as photoanode material instead of a flat semiconductor [23]. When using a nanostrucured photoanode, in fact, a very large number of molecules can be attached to the surface: for example, by using a layer with elevated surface roughness (see Fig. 2.2A) an efficiency of about 1% was obtained [24], but a decisive increment (efficiency value of about 7%) was reached by using a nanostructured material (see Fig. 2.2B). A TCO-covered glass, on which

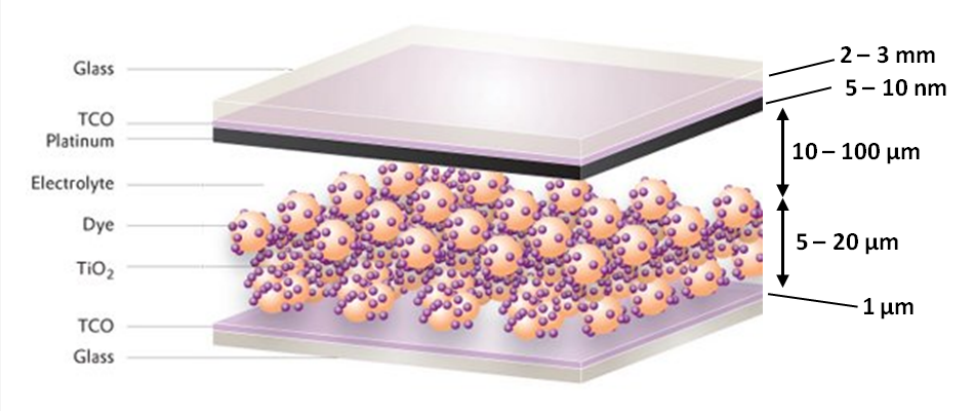

Figure 2.1: DSC architecture (adapted from [25]).

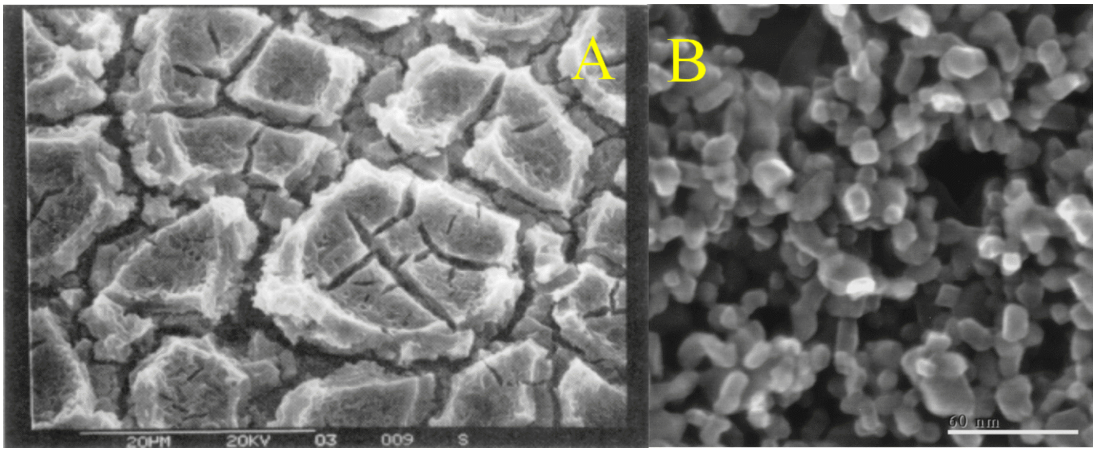

Figure 2.2: Scanning electron micrograph of (A) TiO_2 layer with elevated surface roughness [24] and (B) nanostructured TiO_2 film [26].

a thin film of catalyst is deposited, acts as counter electrode. The catalyst is necessary in order to speed up the charge transfer between electrode and liquid solution. Finally, the role of the electrolytic solution is to conduct holes through a redox couple and regenerate the oxidized dye molecules. This solution fills all the volume between the two electrodes and, thanks to the porous structure of the semiconductor, permits the intimate contact of redox couple with the sensitizer, closing the electrical circuit. In order to close the structure and to prevent electrolyte leakage, a thermoplastic material is placed between the electrodes: it has to be noted that the thickness of the thermoplastic layer defines the electrolyte volume. In the following sections the cell components and their characteristics will be described in details.

2.1.1 Transparent substrates

DSC substrates provide mechanical support for the two electrodes. They are fabricated starting from a glass slice (or a transparent polymer) on which a thin film (about 1 μm-thick) of a TCO is deposited: the role of the conductive film is to allow the charge transfer between the electrodes and the external circuit. The most used TCO materials are the indium tin oxide (ITO), which

is a solid solution of indium oxide (In_2O_3) and tin oxide (SnO_2) with typical 90/10% weight ratio, and the fluorine-doped tin oxide (FTO, SnO_2:F) [27]. Both of them are largely used in the field of solar cells, and they are most commonly deposited on transparent substrates by different *physical vapor deposition* (PVD) techniques; their resistivity is of the order of 10^{-4} Ω·cm. Despite of the lower optical transparency and electrical conductivity (if compared with ITO), FTO is the preferred solution in DSC field, because of the high cost and the limited supply of indium, and the faint flexibility of ITO layers.

2.1.2 Photoanodes

The materials used to fabricate photoanodes are nanostructured oxide semiconductors, with high bandgap (usually higher than 3 eV), that are stable to corrosion and optically transparent in the visible region [4]. The most commonly used material is titanium dioxide (TiO_2) [28], but also other semiconductors have been studied and tested, like zinc oxide (ZnO) [29], tungsten oxide (WO_3) [30] and niobium pentoxide (Nb_2O_5) [31].

Titanium dioxide is historically the first studied material in DSC [19] and has numerous attractive properties, like wide availability, low manufacturing costs, high environmental compatibility and non-toxicity [32]. It can be found in three distinct crystalline forms, namely anatase, rutile and brookite, but in DSC the most used phase is anatase, which exhibits higher conductivity and photoresponse, with a bandgap value of 3.2 eV [33]. Usually in DSC the TiO_2 film is fabricated starting from a paste in which anatase nanoparticles (NPs), with a mean dimension of 20 nm, are dispersed (in Fig. 2.3 scanning electron micrograph, transmission electron micrograph, X-ray diffraction pattern and UV-visible absorbance spectrum of TiO_2 NPs are shown). The oxide paste is deposited onto TCO substrates by means of tape casting or screen printing techniques; then it is subjected to a sintering process in order to enhance the electronic interconnection between the nanoparticles and the charge transfer towards the substrate, and to remove the volatile components of the paste. The NP-based photoanode (with a thickness of about 10 μm) has the great advantage of a high value of SSA (in the range 50 – 250 m^2/g), which permits the anchoring of a great number of dye molecules; however, the charge transport results complicated due to a long pathway for the electron diffusion within the semiconductor network. For this reason there is a growing interest in proposing photoanode materials alternative to NPs, like one-dimensional nanostructures (nanorods [34], nanotubes [35], nanowires [36]) grown exploiting different techniques [37, 38]; these structures are characterized by enhanced transport properties. In Fig. 2.4 some examples of TiO_2 nanostructures are shown.

An interesting alternative to TiO_2 is zinc oxide, a material with an energy gap of 3.37 eV and energetic levels similar to TiO_2. With respect to the latter, ZnO exhibits higher electronic mobility [39] and longer charge lifetime [40]; moreover it can be grown in a wide variety of nanostructures like nanoparticles [29], nanowires or nanorods [41], nanotubes [42] and nanosheets [43]. In spite of these advantages, the photocurrents and the efficiencies of the ZnO cells are still lower than those of TiO_2 NP-based DSCs [44].

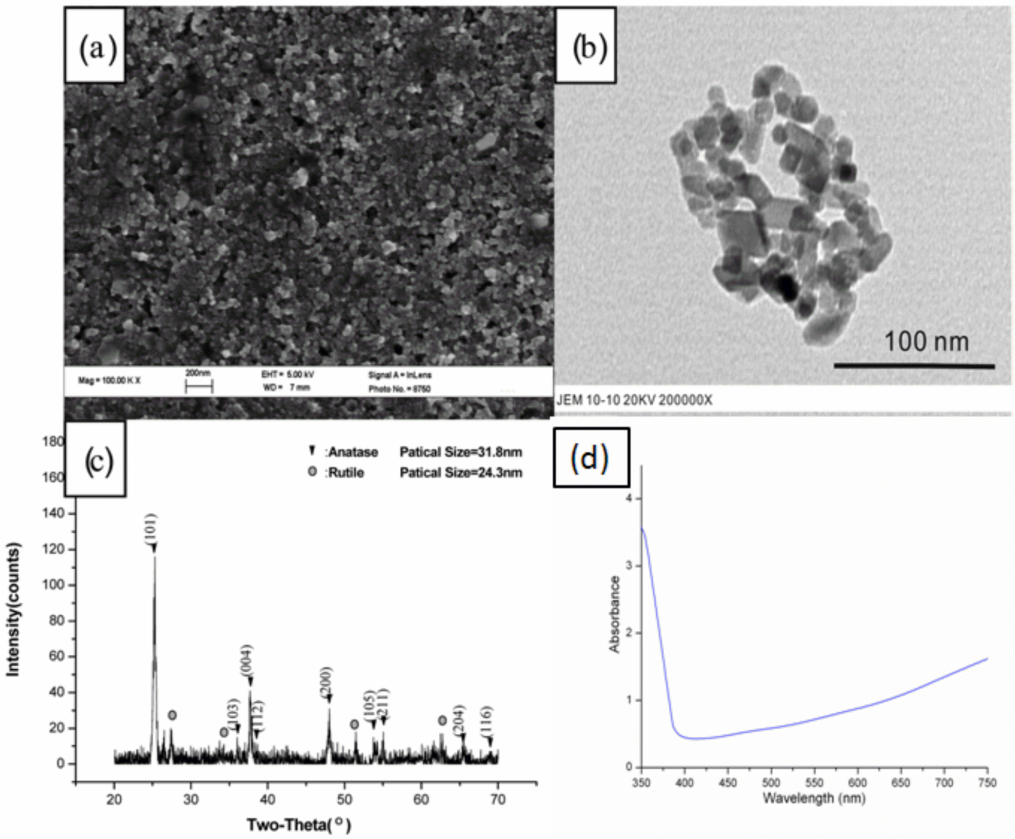

Figure 2.3: Scanning electron micrograph (a), transmission electron micrograph (b), X-ray diffraction pattern (c) and UV-visible absorbance spectrum (d) of TiO_2 nanoparticles (adapted from [45]).

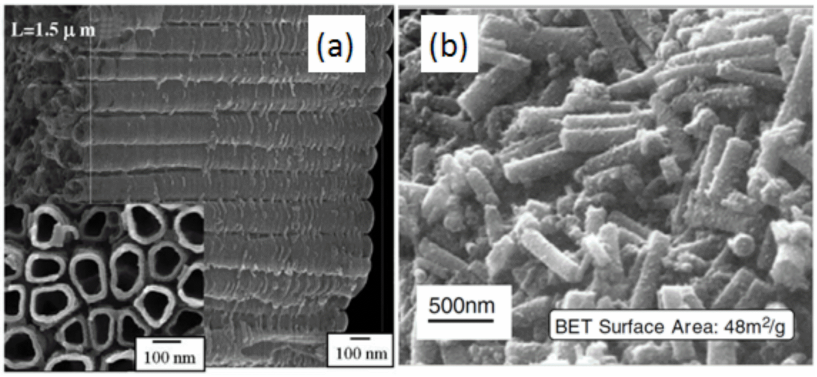

Figure 2.4: Examples of TiO_2 nanostructures: (a) nanotubes [35], (b) nanorods [34].

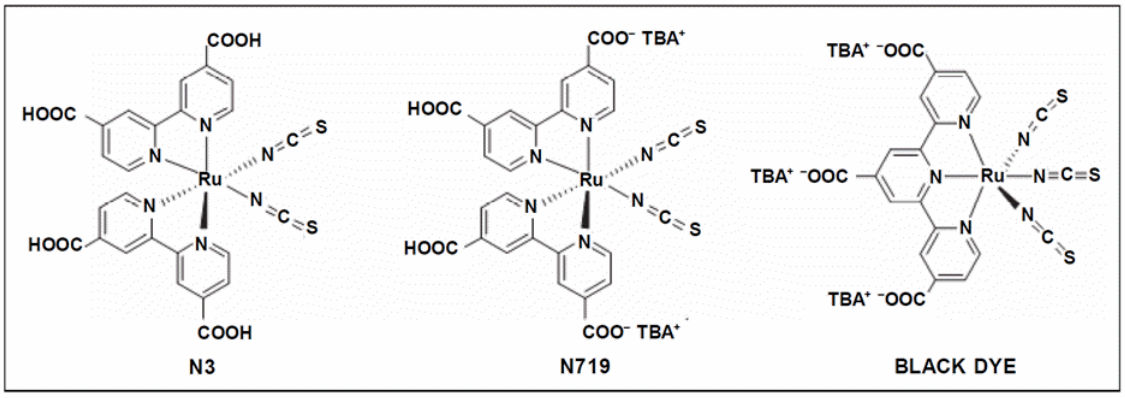

Figure 2.5: Molecular structures of N3, N719 and N749 ("black dye") sensitizers [52].

2.1.3 Sensitizers

The sensitizer is the core element of a DSC: its role is to absorb photons and to generate electrons, which are subsequently injected into the conduction band of the semiconductor on which it is chemisorbed.

Upon absorption of a photon, an electron is promoted from the fundamental state, the Highest Occupied Molecular Orbital (HOMO), to the excited one, the Lowest Unoccupied Molecular Orbital (LUMO). From the highest energetic orbital, if the energetic levels of the LUMO and the semiconductor conduction band (CB) are in favorable positions, the electron can pass into the oxide material. In fact, as will be explained in details in Section 2.2, the excited state of the dye must have a higher energy with respect to the semiconductor conduction band, in order to permit the injection of electrons towards the oxide (the so-called *staggered interface*); moreover the HOMO level needs to have an energy lower than electrolyte redox potential, to allow the dye regeneration [46]. For the mentioned reasons, a particular care has to be devoted to the choice of appropriate dye/semiconductor and dye/electrolyte pairs. Another important characteristic of the sensitizer is its absorption spectrum: in fact, in principle, the higher is the absorption wavelength range, the higher could be the cell efficiency. Moreover the dye should be strongly linked to the oxide in order to obtain a low charge transfer resistance and a stable chemical bond [47]. Finally dye should not incur in aggregation: often dye molecules tend to aggregate each other on the oxide surface, thus increasing the decay from the excited state to fundamental one and consequently reducing the electron injection into semiconductor CB. In order to reduce dye aggregation, some additives are used as co-adsorbent together with sensitizer, such as chenodeoxycholic acid (CDCA) [48].

The sensitizers typically used in DSC belong to two families: metal-organic and organic dyes. Due to employed precursors, synthesis processes and purification steps, the former are characterized by a high cost, but allow to obtain high efficiency values. On the other hand, organic dyes are low-cost and biocompatible, and with a higher molar extinction coefficient, but suffer for lower photovoltaic performances and generally they exhibit higher tendency to molecule aggregation and photo-degradation [49].

Between metal-organic dyes, the most used ones are ruthenium or osmium derivates, which are

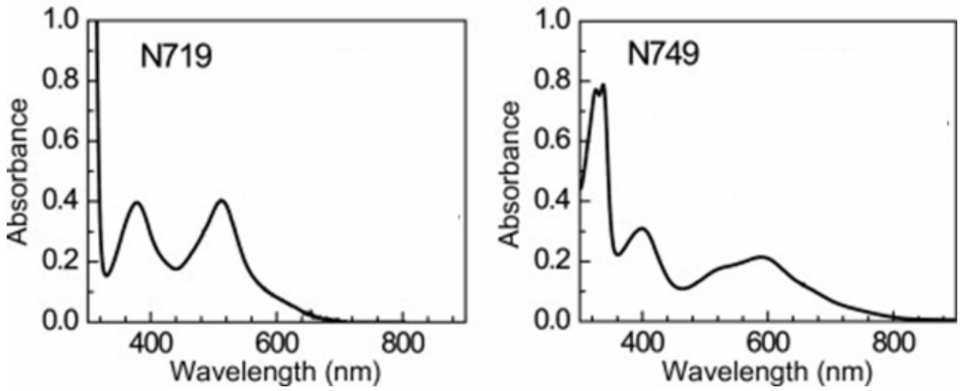

Figure 2.6: Absorption spectra of N719 and N749 dyes in ethanol solution (adapted from [53]).

characterized by prolonged long-term stability. In particular the *polypyridyl ruthenium dye* family allows fabricating DSCs with high conversion efficiency values: in Fig. 2.5 the molecular structures of some ruthenium-based sensitizers are shown. The first developed sensitizer belonging to this group was the RuL_2 $(NCS)_2$ (L = 2,2'-bipyridyl-4,4'-dicarboxylic acid), commonly referred to as N3 dye; its use permits to obtain an energy conversion efficiency as high as 10% [50]. By substituting two protons with a tetra-n-butylammonium (TBA) cation group, the so-called N719 dye was obtained; its formula is [RuL_2 $(NCS)_2$]: 2 TBA. The effect of the deprotonation is to shift the semiconductor conduction band, thus increasing the V_{oc} of the cell (as will be explained in Section 2.2). The enhancement of the open circuit voltage and the subsequent increase of the obtainable PCE made N719 the most common high performance dye [28]. Both N3 and N719-based DSCs exhibit an absorption spectrum in the visible region, with an onset at about 700 nm (see Fig. 2.6a). In order to shift the absorption edge towards IR region, the [RuL'$(NCS)_3$]: 3 TBA (L' = 2,2':6',2"-terpyridyl-4,4',4"-tricarboxylic acid) sensitizer (known as N749 or "black dye") was proposed (see Fig. 2.6b). In Fig. 2.7 the IPCE spectrum of a DSC fabricated with this dye is compared with an N3-based one: it can be clearly seen that the black dye can absorb wavelength up to 900 nm, so the total photocurrent produced can be as high as 20.5 mA/cm^2 [51].

Different families of organic sensitizers have been proposed in the last decade. Between them the most important ones are the coumarin, the indoline, the cyanine and the squaraine dyes (examples of sensitizers belonging to these families are presented in Fig. 2.8). The *coumarin* derivatives were firstly proposed in 2001 [54] with a power conversion efficiency of 5.6%. In 2005 the efficiency of coumarin-based DSC reached 7.4% using NKX-2677 dye [55]. The main disadvantage of coumarin sensitizers, similarly to other organic dye, is the molecule aggregation phenomenon on titania surface. *Indoline* dyes are another class of efficient organic sensitizers, synthesized for the first time by Uchida and co-workers [56]. The most efficient dye belonging to this family is D205; a DSC sensitized with this dye is characterized by a 9.5% efficiency [57]. Another important feature of indoline dyes is their reduced photodegradation that permits a high long-term stability of the cell. *Cyanine* dyes are known for their high molar extinction coefficient values and the capability to absorb the near-IR radiation [58]. However the photovoltaic performances of DSC based on these dyes are quite low: for example using the Cy3 dye, a 4.8% of PCE under 75

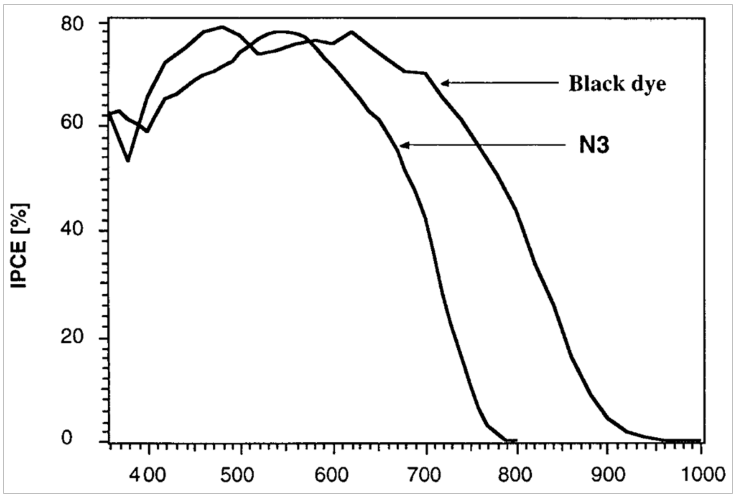

Figure 2.7: Incident photon-to-electron conversion efficiency of DSCs sensitized by N3 and N749 ("black dye") dyes (adapted from [26]).

mW/cm^2 illumination has been obtained [59]. Representative sensitizers of the *squaraine* family are SQ1 and SQ2 dyes, proposed by Grätzel and co-workers [60, 61], which are characterized by relatively high conversion efficiencies (4.5% and 5.4% respectively), high molar extinction coefficient values and strong electronic coupling with TiO_2 surface. However the squaraine photovoltaic performances are limited by the dye aggregation.

Sometimes, when using organic dyes, whose absorption spectrum is usually narrower with respect to metal-organic ones, the so-called *co-sensitization* strategy can be used in order to increase the DSC performances: different organic dyes (each absorbing in a distinct wavelength range) can be chemisorbed on the same semiconductor layer, thus obtaining a *panchromatic* absorption. An efficient example of co-sensitization is represented by SQ1 dye (that absorbs in red and near-IR regions) and JK2 dye (that absorbs in visible region) [62]: the DSC IPCE spectrum of Fig. 2.9 shows a photocurrent generation between 370 and 700 nm, thus demonstrating the panchromatic absorption.

2.1.4 Counter electrodes

As photoanodes, also counter electrodes are fabricated starting from a glass covered with a film of conductive oxide. In order to have a fast reduction reaction kinetics at cathode a catalyst is deposited onto TCO [28]. The most used catalysts in DSCs are platinum and graphite.

The use of Pt assures high values both of current and voltage, and is characterized by low counter electrode resistance [63]; it can easily deposited through thermal evaporation [64], sputtering [65], or thermal decomposition of H_2PtCl_6 [66]. The main disadvantage of the Pt is the high cost of the material.

Graphite represents a low-cost solution for counter electrode fabrication [67]. The main issues with this material are the low homogeneity and adhesion to the substrate, so the performance of the cells based on this catalyst are lower with respect to the Pt-based ones [16].

Another low-cost solution is the use of conducting polymers deposited onto TCO, like doped

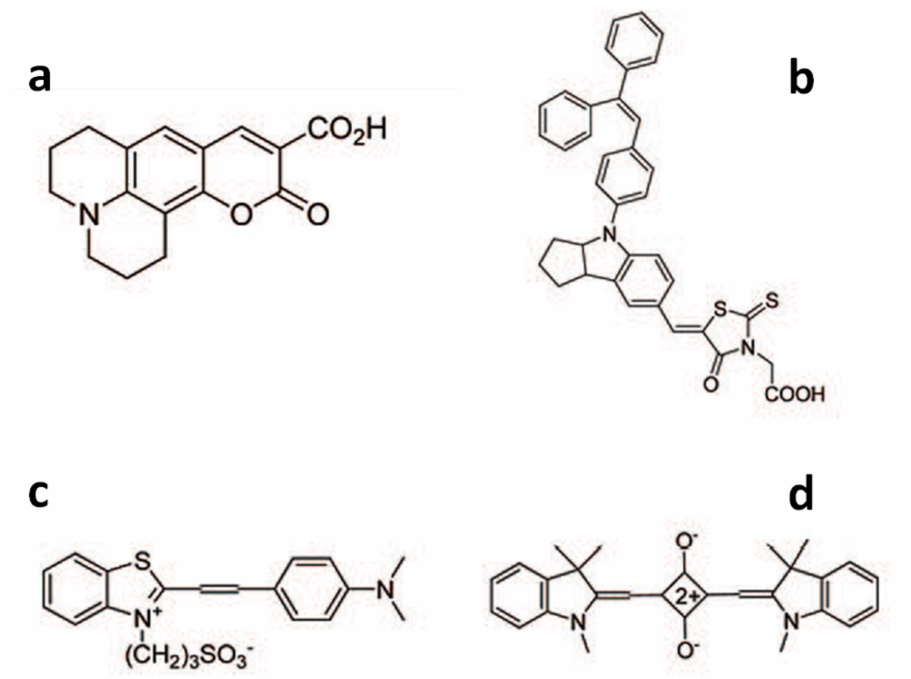

Figure 2.8: Molecular structures of dyes belonging to different families of organic sensitizers: a) coumarin, b) indoline, c) cyanine and d) squaraine (adapted from [28]).

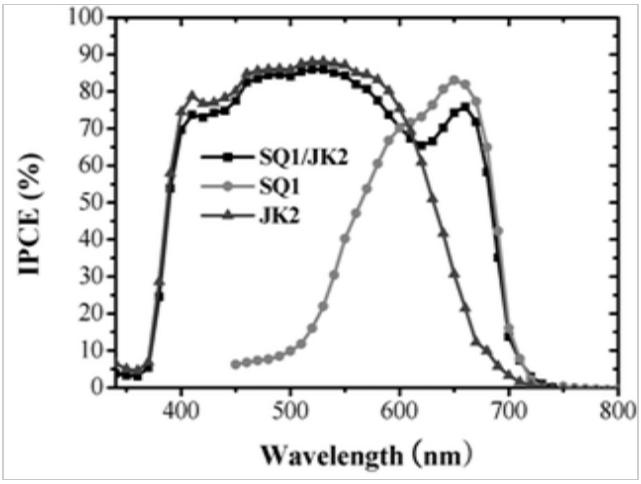

Figure 2.9: Incident photon-to-electron conversion efficiency of a DSC co-sensitized by SQ1 and JK2 dyes. For comparison the relative spectra of DSCs sensitized by SQ1 and JK2 dyes are reported (adapted from [62]).

poly(3,4-ethylenedioxythiophene) (PEDOT), which shows good catalytic properties for the reduction of triiodide [68].

An interesting alternative material is graphene, which in principle could act as transparent conductive film and catalyst at the same time, thus reducing the counter electrode fabrication cost. Interesting results have been published so far [69, 70], evidencing high conductivity values.

2.1.5 Electrolytes

The most common class of electrolyte used in DSCs is the liquid solvent-based one. They are usually constituted by a redox couple dissolved in an organic solvent; moreover some additives can be inserted in order to increase the device performances [28].

Since the redox couple is responsible for the dye regeneration, as already mentioned in Section 2.1.3, its redox potential must be higher than dye HOMO level. Moreover it has to satisfy the following requirements [71]:

- it has to be high soluble in the solvent used;
- its diffusion coefficient in the solution has to be high in order to grant good transport properties (in DSC the hole transport is a diffusion-driven process);
- both the reduced and oxidized forms of the couple have to be thermally and electrochemically stable, and the reaction needs to be chemically reversible;
- it should be chemically inert towards other components of the cell;
- its reaction with electrons present in TiO_2 and TCO (*back reaction*) has to be faint in order to limits unwanted charge recombination (see Section 2.2.1);
- the solution must be transparent in the visible region.

The most used redox couple is iodide/triiodide (I^-/I_3^-), mainly because of the slow recombination reaction; electrolytes based on this couple are usually prepared by dissolving iodide salts with different cations (Li^+, Na^+, Mg^+) in the liquid solvent. However the corrosive properties of iodine are the principal reason for the search of alternative redox couples, like Br^-/Br_3^-, $SCN^-/(SCN)_3^-$ and $SeCN^-/(SeCN)_3^-$, which have promising electrochemical and non-corrosive properties, but suffer for chemical instability [28]. Very recently, through the use of cobalt(II/III)tris(bipyridyl) redox couple an impressive efficiency of 12.3% has been obtained, which represents so far the highest efficiency for a DSC [72].

Concerning the solvent, it must have low volatility in the operating DSC temperature range, low viscosity in order to allow the fast diffusion of charges, and a high dielectric constant to make the redox couple dissolution easier [28]. Between all the solvent used in DSC, acetonitrile (ACN) is considered the best performing one, due to its excellent stability, low viscosity and capability of dissolve a lot of salts and organic molecules; its use grants high values of cell efficiency, so it is mainly used for tests on sensitizers [73]. Unfortunately ACN boiling point is low (78 °C), so for

long-term stable cell application the preferred choice is 3-methoxypropionitrile (MPN), characterized by 164 °C boiling point and low toxicity: an efficiency of 7.6% after 1000 h of continuous irradiance has been obtained using MPN as solvent [74]. Less used solvents are water, ethanol, ethylene carbonate and propylene carbonate [73].

Regarding the additives, a lot of cations and compounds have been used in order to enhance the photovoltaic performances of the cell. Between them, the most employed one is the 4-tert-Butylpyridine (TBP), whose effect is to increase the open circuit voltage thanks to the shift of TiO_2 conduction band towards higher energy (as will be explained in Section 2.2, the V_{oc} value is defined as the difference between the quasi-Fermi level of the electrons in the titanium dioxide film and the redox potential of the electrolyte) [75]. The addition of guanidinium thiocyanate (GuSCN) in the liquid electrolyte leads to an increase of both current and voltage, due to a positive shift of the TiO_2 CB and a reduction of charge recombination [76].

The main issue when using liquid solvent-based electrolyte is the evaporation that limits the device long-term stability, and makes necessary the use of some cell sealing in order to reduce this phenomenon. Moreover the use of these electrolytes is hardly compatible with industrial production processes, like the so-called *roll-to-roll* technique. To overcome these problems, different alternative solutions have been proposed and are currently under study. Between them we can find the solvent-free liquid electrolytes, the quasi-solid electrolytes and the solid electrolyte. The former are based on ionic liquids and are characterized by reduced volatility, but with a higher viscosity that slow down the charge diffusion [77]. Quasi-solid electrolyte can be obtained starting from organic solvent-based or ionic liquid electrolytes that can be gelated, polymerized, dispersed in polymeric matrix, or in which nanoparticles are dispersed [28]. Solid-state electrolytes are represented by polymer or organic p-type conductor, like polypyrrole [78], poly(3,4-ethylenedioxythiophene) (PEDOT) [79] or poly(3-hexylthiophene) (P3HT) [80]. However the photovoltaic performances of DSCs based on all these alternative electrolytes are currently lower with respect to the liquid solvent-based ones, so further work is needed.

2.1.6 Sealing

As already reported in the previous section, one of the main problems concerning the use of liquid electrolyte is the solvent evaporation.

For quick laboratory tests there is no need of a perfect cell closure, so in these cases the DSC can be assembled simply sandwiching the two electrodes using clips, and the electrolyte filling is obtained by soaking up a droplet between the glass slices. However this assembly procedure does not grant a good degree of fabrication reproducibility, since the electrolyte volume is not a fixed parameter [64].

For the above reasons, a rigorous sealing procedure is often adopted, but it appears to represent the biggest technological challenge for the production of this kind of devices. The sealing is usually performed with an epoxy resin [50], polyester [81] or glue [23]. In these cases, however, the cell assembly process became more time consuming. In fact, after the structure sealing, the electrolyte has to be inserted by means of a vacuum procedure, which consists in pouring an

electrolyte droplet on the top of a hole drilled on the counter electrode and evacuating the free space between the electrodes, thus allowing the electrolyte to completely fill the volume [20].

2.2 Principle of operation

The basic electron transfer processes in a DSC, as well as the potentials for a DSC based on the N3 dye, TiO_2 as photoanode material and I^-/I_3^- as redox couple, are presented in Fig. 2.10. Photoexcitation of the dye (process 0) results in the injection of an electron into the conduction band of the oxide (process 2), leaving the dye in its oxidized state. Injected electron travels through the semiconductor reaching the conductive substrate (process 4), thus flowing in the external circuit. The dye is restored to its ground state by electron transfer from the electrolyte (process 3). The I_3^- ions formed by oxidation of I^- diffuse through the electrolyte to the cathode where the regenerative cycle is completed by electron transfer to reduce I_3^- to I^- (process 7). By looking at the energetic levels of dye, semiconductor conduction band and electrolyte redox potential, is it clear that for an efficient operation of this kind of device the dye LUMO must have an energy higher than oxide CB and the HOMO should be lower with respect to redox potential: for the above reasons the sensitizers have to be designed and synthesized in the appropriate way, to match the energy requirements of semiconductor and redox couple. The voltage generated under illumination corresponds to the difference between electrochemical potential of the electron at the two contacts, which generally for DSC is the difference between the Fermi level of the mesoporous TiO_2 layer and the redox potential of the electrolyte [22]. For a DSC to be durable for more than 15 years in outdoor conditions, the entire process has to be repeated 10^8 times (*turnover number*) and the electric power must be generated without permanent chemical transformation: the ruthenium complexes dye described on Section 2.1.3 can satisfy these requirements [82]. However, some unwanted reactions resulting in losses in the cell efficiency can occur, and these processes are also indicated in Fig. 2.10. Process 1 is the direct recombination of the excited dye (reflected by the excited state lifetime). Recombination of injected electrons in the TiO_2 with oxidized dyes or with holes in the electrolyte is indicated as 5 and 6, respectively. In principle, this last process could occur at the interface between the oxide and the electrolyte or in those regions of TCO that are not covered by the semiconductor (that are therefore directly exposed to the electrolyte); practically, this second recombination route can be suppressed by using a compact blocking layer of oxide deposited on the substrate [83].

The charge transfer processes presented above will be discussed in details in the following section.

2.2.1 Charge transfer processes

Upon absorption of a photon with frequency ν, the sensitizer passes from its ground state S to the excited one S^* (process 0 in Fig. 2.10) following the reaction:

$$S + h\nu \rightarrow S^* \tag{2.1}$$

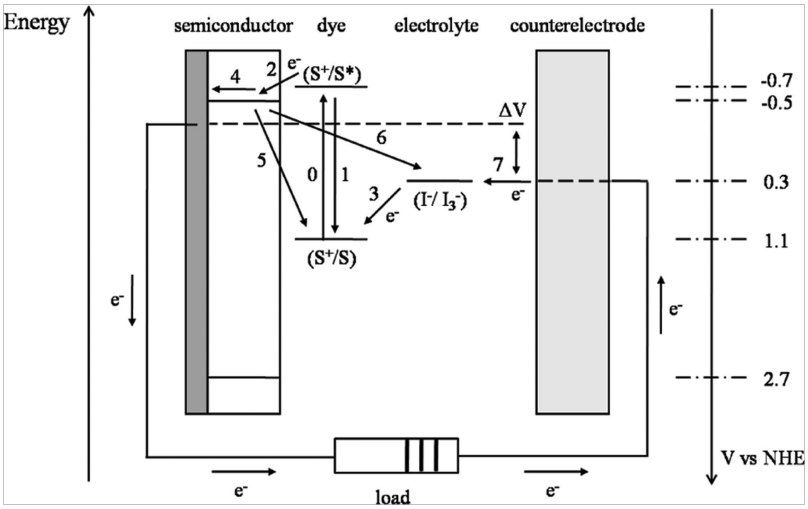

Figure 2.10: Simplified energy level diagram for a DSC based on N3 dye, TiO_2 photoanode and I^-/I_3^- redox couple. The basic electron transfer processes are indicated by numbers (0 – 7) [28].

The second step is the injection of an electron into the CB of the semiconductor, thus leaving the sensitizer in the oxidized state S^+ (process 2, Eq. 2.2):

$$S^* \rightarrow S^+ + e^-_{(TiO_2)} \tag{2.2}$$

The detailed mechanism of the injection process is currently not fully comprised and it is still under investigation, but it is generally accepted that it occurs in the femtosecond time scale for Ru-complex sensitizer attached to an oxide surface [84]. For good device performances, the duration of the injection process should be compared with the decay of the excited state of the dye to the ground state (process 1). This is given by the excited state lifetime of the dye, which for typical Ru-complexes used in DSCs is 20 – 60 ns [85]: by looking at these values, it can be assert that for this kind of dye the injection is an ultrafast process. However, for an efficient device, it is important that also the quantum efficiency for injection is high. The electron injection efficiency is defined as follows:

$$\eta_{inj} = \frac{k_{inj}}{k_{inj} + k_d} \tag{2.3}$$

where k_{inj} and k_{d} are the rate constants for electron injection and decay (radiative and nonradiative) of the excited dye, respectively; for efficient injection, k_{inj} should be about 100 times larger than k_{d}. A possible way to enhance η_{inj} (and so J_{sc}) is to decrease the conduction band energy E_{C}: however this shift would lead to a decrease of open circuit voltage (see Section 2.2). Since the optimization of a DSC is achieved by maximizing the electrical power output, that is, the product of current and voltage, there will be always a compromise value for η_{inj}: for example, even if N719 dye is characterized by a 30-fold slower rate of injection as compared with N3 dye [86], the increase of V_{oc} is responsible for the higher photoconversion efficiency of N719-based DSCs.

The regeneration of the oxidized dye by the electron donor, normally I^- (process 3), is in the microsecond time domain. The corresponding reaction is:

$$S^+ + \frac{3}{2}I^- \rightarrow S + \frac{1}{2}I_3^- \tag{2.4}$$

Considering a turnover number of 10^8, the lifetime of the oxidized dye must be higher than 100 s if the regeneration time is 1 μs [87].

The charge transport through the mesoporous layer (process 4) is surely a highly efficient process, which occurs in the millisecond range; however it is not fully comprised. The oxide film may be viewed as an ensemble of individual particles through which electrons can percolate by hopping. Since these particles are typically not electronically doped and are surrounded by ions in the electrolyte, they will not have an internal electrical field and will not display any significant band bending; moreover, the photoinjected electrons are charge compensated by ions in the electrolyte. For these reasons, the gradient in electron concentration seems to be the main driving force for transport in the mesoporous TiO_2 film, that is, electron transport occurs by diffusion [88]. However, in contrast to this, it has been observed that the electron transport depends in a non-linear way on the incident light intensity (it becomes faster at higher light intensities). Considering a diffusion coefficient that is light-intensity dependent or, more correctly, dependent on the electron concentration and Fermi level in the TiO_2, a multiple trapping (MT) model have been developed to describe the electron transport [89]. In this model, electrons are considered to be mostly trapped in localized states below the conduction band, from which they can escape by thermal activation. By studying the electron transport using small-modulation methods (see Section 3.3), a chemical *diffusion coefficient* (D_n) is determined. With a quasi-static approximation in the MT model, the following expression was derived for D_n [89]:

$$D_n = \left(1 + \frac{\partial n_T}{\partial n_C}\right)^{-1} D_0 \tag{2.5}$$

where n_T and n_C are the concentrations of trapped and conduction band electrons, respectively, and D_0 is the diffusion coefficient of conduction band electrons. The precise nature and location of the traps in the mesoporous TiO_2 is still a subject of discussion, but it is generally accepted that the traps that are involved in electron transport in DSCs can be located either in the bulk, at grain boundaries, or at the oxide/electrolyte interface. The kinetics of the back-electron transfer reaction from the semiconductor CB to the oxidized sensitizer (process 5, Eq. 2.6) follow a multi-exponential time law, occurring on a microsecond to millisecond time scale (depending on electron concentration in the semiconductor and thus on the light intensity). The recombination of electrons in TiO_2 with acceptors in the electrolyte (process 6, Eq. 2.7) is usually referred to as the *electron lifetime* (τ_n). Lifetimes observed with the I^-/I_3^- are very long (1 – 20 ms under one sun light intensity) compared with other redox systems used in DSC, thus explaining the diffused usage of this redox couple.

$$S^+ + e^-_{(TiO_2)} \rightarrow S \tag{2.6}$$

$$I_3^- + 2e^-_{(TiO_2)} \rightarrow 3I^-_{(anode)} \tag{2.7}$$

These two routes of recombination are possible in DSC because during their transport through the mesoporous TiO_2 film constituted of nanometer-sized particles, electrons are always within only a few nanometers distance from the semiconductor/electrolyte interface. In particular, the recombination of electrons with oxidized dye molecules can compete with the regeneration process, both occurring on the same time scale, especially under actual working conditions. In fact, when the electron concentration in the TiO_2 particles is increased, a strong increase in recombination kinetics is found [88]. In this case, it is useful to define the regeneration efficiency, η_{reg}, which gives the probability that an oxidized dye is regenerated by an electron donor in the electrolyte rather than by recombination with an electron in the TiO_2:

$$\eta_{reg} = \frac{k_{reg}}{k_{reg} + k_{rec}} \tag{2.8}$$

here k_{reg} is the rate constant for regeneration and k_{rec} is the first-order rate constant for electron-oxidized dye recombination. For many types of sensitizer, very high η_{reg} values, approaching unity, have been found with iodide, which represents the most used electron donor. Fast regeneration kinetics were also found for one-electron redox mediators: $[Co(dbbip)_2]^{2+}$ gave regeneration times of some microseconds and regeneration efficiencies higher than 0.9 [90]. Regarding the recombination of electrons in TiO_2 with acceptors in the electrolyte, this phenomenon can be in competition with the transport through the oxide, being in same time range. In order to have an efficient energy production, the oxide *transport time* τ_{t} should be lower than electron lifetime: in this case the electrons are able to reach the front electrode before recombination occurs. Often the transport properties are summarized through the *diffusion length* L_{n}, which is the square root of the product of the electron lifetime and diffusion coefficient:

$$L_n = \sqrt{\tau_n D_n} \tag{2.9}$$

if this parameter is greater than the film thickness, all of the photogenerated carriers will be statistically collected [23].

Transport of the redox mediator between the electrodes is mainly driven by diffusion, and it is characterized by an *electrolyte diffusion impedance*, which acts as a series resistance in the solar cell. This impedance depends on the diffusion coefficient and concentration of the redox mediator, and on the distance between the electrodes, with values of the order of 2 Ω/cm^2 [91], leading to characteristic times above 1 s. At the counter electrode, in standard DSCs, triiodide is reduced to iodide, following the reaction (process 7)

$$I_3^- + 2e^-_{(cathode)} \rightarrow 3I^-_{(cathode)} \tag{2.10}$$

whose duration is of the order of the milliseconds. The counter electrode must be catalytically active to ensure rapid reaction and low overpotential: as already mentioned in Section 2.1.4, Pt is the most used catalyst. The charge transfer reaction at the counter electrode leads to a series resistance in the DSC, the so-called *counter electrode charge transfer resistance* R_{CE}. Ideally, R_{CE} should be lower than 10 $\Omega \cdot cm^2$ to avoid significant losses [63]. A poor counter electrode will

affect the current-voltage characteristic of the DSC by lowering its fill factor.

Chapter 3

DSC characterization techniques

This chapter is dedicated to the description of the techniques that are commonly used to characterize the photovoltaic performances and the charge transport and recombination properties of DSCs. The former are usually evaluated by means of the already introduced current - voltage and incident photon-to-electron conversion efficiency measurements, so both techniques will be presented. The charge transfer properties are instead evaluated exploiting different methods, for example by light modulation or by voltage modulation; since only the last approach was exploited in this work, the intensity modulated photocurrent spectroscopy and intensity modulated voltage spectroscopy will be briefly described, while particular attention will be given to open circuit voltage decay and electrochemical impedance spectroscopy techniques.

3.1 Current - Voltage

As already mentioned in Section 1.2, the standard method used to evaluate the photovoltaic performances of a solar cell is to measure its current - voltage (I-V) characteristic. In order to compare the results obtained by various research groups all over the world, I-V measurements are usually performed under standard AM1.5G condition (see Section 1.1).

The standard set-up is constituted by a solar simulator that provides the illumination (usually through the use of a Xe lamp and an AM1.5G optical filter) and a Source Measure Unit (SMU) that applies the bias voltage to the cell and acquires the corresponding current value. Starting from I-V curves, the photovoltaic parameters can be evaluated by using Eqs. 1.2 and 1.3. However, differently for what happens with standard Si-based solar devices, DSC characterization requires particular cares in measurement conditions, namely the direction of the voltage scan (forward or reverse), the delay time between two consecutive bias voltages and the use of a mask [92].

3.2 Incident Photon-to-electron Conversion Efficiency

The measurement of the Incident Photon-to-electron Conversion Efficiency spectrum is important in order to acquire information about the electrical response of the cell for different incident wavelengths. This kind of characterization is particularly useful for the testing of sensitizers, because it allows knowing the wavelength range in which dye molecules are able to absorb and efficiently inject electrons into TiO_2 conduction band.

The set-up that is usually used to perform this kind of measurement on common (i.e. silicon-based) solar devices is constituted by a lamp whose output passes through a chopper and it is sent to a monochromator, then the output beam impinges on the cell under test; the device is also illuminated by a lamp with constant output, in order to keep it under normal working conditions. The short circuit current density produced by the cell in response to the sum of monochromatic and constant illumination is acquired through a lock-in amplifier that selects only the AC component related to the monochromatic beam $J_{sc}(\lambda)$. If the incident light power density at each wavelength $\phi(\lambda)$ is known, the IPCE value at a given wavelength can be evaluated by using the formula [93]:

$$IPCE = 1240\frac{J_{sc}(\lambda)}{\lambda\phi(\lambda)} = \eta_{lh}(\lambda)\eta_{inj}(\lambda)\eta_{coll}(\lambda) \tag{3.1}$$

where J_{sc} is measured in mA/cm^2, ϕ in mW/cm^2, λ in nm, and η_{lh}, η_{inj} and η_{coll} have already been defined in Section 1.2. The chopping frequency usually adopted in the measurement of Si-based devices is of the order of different tens of Hz, in order to obtain stable and noise-free signals. These values are suitable for p-n junction based devices because their response time is of the order of 1 ms, but can create problems for the IPCE evaluation of DSCs because their response time can be as long as 1 s, especially for low light illumination condition [94]. Very few papers have been published so far concerning this topic, but different viewpoints are presented [45, 94, 95]. Recently an alternative method to perform IPCE measurement exploiting continuous monochromatic irradiation (i.e. without chopping and without additional bias light) has been proposed [96]: in this case the current is simply acquired through the use of a SMU. This method has proven to be reliable for IPCE measurement of DSCs, if the evaluation of the current for a given wavelength is done after a sufficient long time (3 s), in order to ensure that the J_{sc} had reach a steady-state value before acquiring it [94, 97].

3.3 Intensity Modulated Photocurrent Spectroscopy and Intensity Modulated Voltage Spectroscopy

Since in DSCs the charge transport and recombination exhibit a nonlinear dependence on the light intensity (as reported in Section 2.2.1), one of the best method used to study these processes is to illuminate the devices with a small perturbation of light intensity superimposed to a larger constant light intensity. Rapid modulation of light can be easily obtained by using light-emitting diodes (LEDs) or laser-diodes.

The Intensity Modulated Photocurrent Spectroscopy (IMPS) technique is based on a sinu-

soidal modulation of the incident light intensity: the resulting short circuit photocurrent response is measured as a function of the modulation frequency by using phase-sensitive detection [98], similarly to electrochemical impedance spectroscopy (see Section 3.5). Through this technique, is it possible to evaluate the time constant for photocurrent response, τ_{pc}, which depends on both electron transport and electron recombination, according to the following equation [99]

$$\frac{1}{\tau_{pc}} = \frac{1}{\tau_t} + \frac{1}{\tau_n} \tag{3.2}$$

Since in DSC with iodide/triiodide-based electrolyte under short circuit conditions τ_n is usually much larger than τ_t, the measured photocurrent response time is practically equal to the transport time. In this case, the chemical diffusion coefficient can be calculated from the electron transport time using Eq. 3.3

$$D_n = \frac{d^2}{C\tau_t} \tag{3.3}$$

where d is the thickness of the mesoporous TiO_2 film and C is a constant with a value of about 2.5, which depends slightly on the absorption coefficient of the film and on the direction of illumination [100].

In a similar way electron lifetime measurements are usually performed through Intensity Modulated Voltage Spectroscopy (IMVS), with the difference that the open circuit potential is monitored instead of the short circuit photocurrent [101]. Under open circuit condition, the photogenerated electrons are not extracted at the front contact but will recombine with holes in the electrolyte; the characteristic response time obtained by small-modulation light intensity corresponds to the electron lifetime.

In Fig. 3.1 the typical plots derived from IMVS and IMPS measurements for a DSC are reported.

3.4 Open Circuit Voltage Decay

The Open Circuit Voltage Decay (OCVD) method is an experimental technique specifically developed for DSCs [102]. Basically, it is an indirect measurement of the electron lifetime, but, differently from IMVS, the OCVD allows obtaining information about charge recombination with high voltage resolution, and also it is experimentally simpler.

The initial step of the measurement is the constant illumination of the cell under open circuit condition until a non-equilibrium steady state is reached. Then the illumination is interrupted and the voltage is recorded as a function of time while maintaining the cell at open circuit. During the decay, since the device is at open circuit and no current can flow through the external circuit, the photoelectrons initially present in the oxide conduction band recombine (see Section 3.3), thus reducing their value until a dark equilibrium state with a concentration n_0 is reached (and V_{oc} = 0). In the approximation of first order recombination, this decay assumes an exponential behavior, and it is possible to calculate the electron lifetime through the formula [102]:

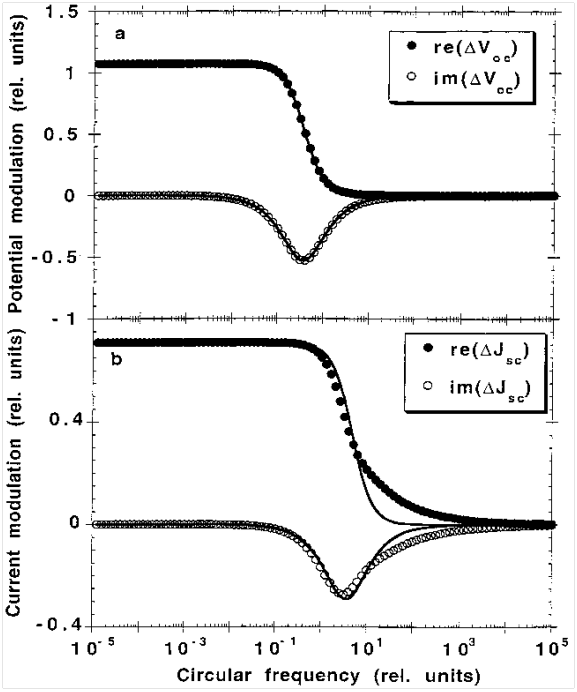

Figure 3.1: Typical IMVS (a) and IMPS (b) response of a nanocrystalline DSC [99].

$$\tau_n = -\frac{k_B T}{q}\left(\frac{dV_{oc}}{dt}\right)^{-1} = -V_{th}\left(\frac{dV_{oc}}{dt}\right)^{-1} \tag{3.4}$$

where k_B is the Boltzmann constant, T is the absolute temperature and q is the elementary charge value, and the quantity $V_{th} = k_B T/q$ is called *thermal voltage* (approximately equal to 25 mV at room temperature). However at the moment the recombination mechanisms are not fully understood, and the possibility of a non-linear recombination reaction has been proposed [103]. If γ is the effective recombination order, it can be calculated starting from the $\tau_n(V_{oc})$ curve as follows:

$$\gamma = 1 + \frac{k_B T}{q}\frac{d(ln\tau_n^{-1})}{dV_{oc}} \tag{3.5}$$

Nevertheless it has been proved that if the γ values are quite close to unity the approximation leading to Eq. 3.4 can be used. In practical cases, γ values of about 1.3 have been found, so the electron lifetime can be calculated starting from OCVD measurement through this equation [102]. In Fig. 3.2 an example of V_{oc} decay results for different initial illumination conditions is proposed, and the corresponding $\tau_n(V_{oc})$ curves are reported.

In literature, an excellent accordance between the electron lifetime values obtained by this method with the ones evaluated by IMVS measurements is generally reported, thus proving the reliability of OCVD technique [102].

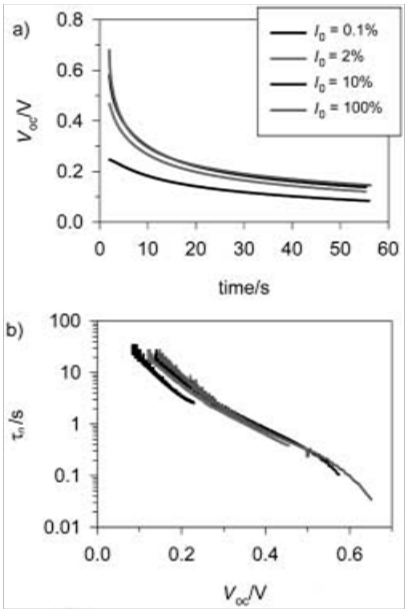

Figure 3.2: a) Example of open circuit voltage decay measurement for different initial illumination conditions (indicated by the relative incident light intensities). b) Corresponding electron lifetime curve evaluated through Eq. 3.4 (adapted from [102]).

3.5 Electrochemical Impedance Spectroscopy

Electrochemical Impedance Spectroscopy (EIS) is a well-established technique, widely used for the study of electrochemical devices and systems, being at the same time a simple but powerful tool; this technique is based on the analysis of the electric response of a cell to an applied periodic voltage of variable frequency superimposed to a constant bias voltage [77, 104].

In electrochemical cells, the transport and charge-transfer processes are described by nonlinear equations connecting the driving forces to the flux of the particles. When the amplitude of the applied voltage is comparable with the thermal voltage (i.e. under small signal condition), the fundamental equations describing the charge redistribution in the cell due to the external voltage are linear. In this approximation, it is possible to describe all the processes by linear equations in which the coefficient between the electrochemical potential and the current is the electric impedance. For a DSC, since the different transport and recombination processes occurring in the device are characterized by quite different time constants, this technique permits to distinguish all these mechanisms: the diffusion-recombination electronic processes in the TiO_2 layer and at the semiconductor/electrolyte interface, the diffusion mechanism of the redox species in the electrolyte, and also the charge transfer at the counter electrode [105]. In this framework, the electrochemical cell behavior can be described by an equivalent electric circuit. Usually the shape of the I-V curve of a DSC can be fitted quite well exploiting the simple diode circuit model reported in Fig. 3.3 corresponding to the following equation:

$$i_{CELL} = i_{ph} - i_0 \left(e^{-\frac{V_{CELL}+i_{CELL}R_s}{mV_{th}}} - 1 \right) + \frac{V_{CELL}+i_{CELL}R_s}{R_{sh}} \tag{3.6}$$

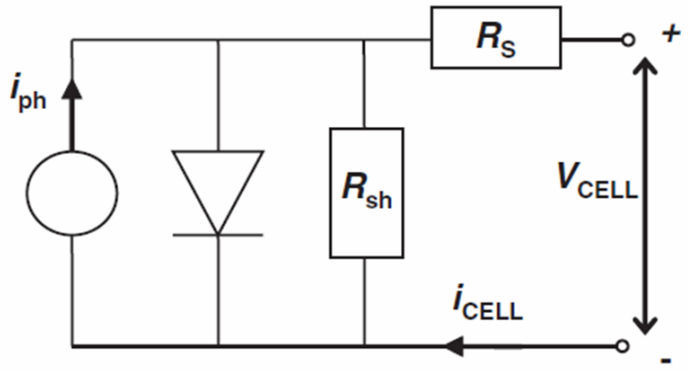

Figure 3.3: Basic diode equivalent circuit model of a solar cell [106].

where i_{ph} is the photocurrent modeled as an ideal current generator, i_0 the diode reverse saturation current (the so-called *dark current*), m is the diode ideality factor, and R_s and R_{sh} are the series and shunt resistances of the cell. All these parameters can be determined by fitting the model to a measured solar cell I-V curve. However, in the fitting process R_s needs to be assumed constant, but this is not the case in DSCs, because the series resistance takes into account also the contributions from the current-dependent resistances of charge transfer and mass transport at the counter electrode [106]. For this reason the modeling circuit that is usually adopted to fit the EIS data (the *transmission line model*, TLM) is more complicated, and it will be presented in the next section. In Section 3.5.2 the typical features exhibited by an EIS measurement on a DSC will be discussed.

3.5.1 The transmission line model

Fig. 3.4 shows the widely used equivalent circuit model of DSC. In this picture, the representation of the nanostructured oxide has been simplified to a columnar model that represents the mesoporous layer (with thickness d) in which the electrolyte solution interpenetrates. The circuit components and their units are [107]:

- R_S (Ω): *ohmic series resistance* of the cell, accounting for the sheet resistance of the TCO substrates, and electrical contacts and wiring of the cell.
- R_{CO} (Ω): *substrate contact resistance* at the interface between the TCO and the TiO_2 film.
- C_{CO} (F): *substrate contact capacitance* at the interface between the TCO and the TiO_2 film.
- R_{TCO} (Ω): *substrate charge transfer resistance* accounting for electron recombination from the uncovered layer of the TCO to the electrolyte.
- C_{TCO} (F): *substrate double layer capacitance* at the TCO/electrolyte interface.
- r_t (Ω/m): *electron transport resistance* in the semiconductor layer. The total transport resistance of the film is $R_t = r_t \cdot d$.

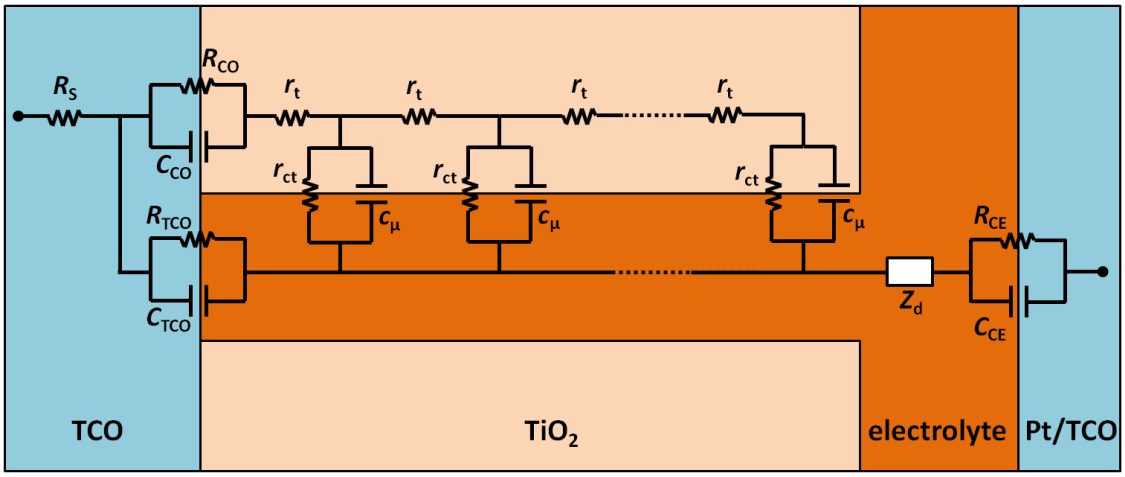

Figure 3.4: Equivalent circuit based on the transmission line model for a DSC.

- r_{ct} (Ω·m): *recombination charge transfer resistance* at the TiO_2/electrolyte interface. The total recombination resistance of the film is $R_{ct} = r_{ct}/d$.
- c_μ (F/m): *photoanode chemical capacitance*, that stands for the change of electron density as a function of the Fermi level. The total chemical capacitance is $C_\mu = c_\mu \cdot d$.
- Z_d (Ω): *electrolyte diffusion impedance*, accounting for mass transport of redox species in the electrolyte.
- R_{CE} (Ω): *counter electrode charge transfer resistance* at the Pt/electrolyte interface.
- C_{CE} (F): *counter electrode double layer capacitance* at the Pt/electrolyte interface.

Usually two assumptions can be made in order to simplify the above presented circuit [106]. First of all, the electron recombination through the TCO layer can be neglected if compared to the one occurring at oxide/electrolyte interface; this usually happens at normal light intensity (of the order of 1 sun) and also at low-intensity when a blocking layer is present onto the TCO substrate (as explained in Section 2.2). Regarding the interface between the substrate and the oxide layer, it can be assumed that the contact has negligible resistance, since the effects of non-zero R_{CO} is present only for certain recombination blocking layer use or when ITO is present instead of FTO. Moreover, the ideal capacitors present in the circuit are often replaced by the *Constant Phase Elements* (CPEs) that are generalization of conventional capacitances included to take into account frequency dispersion that can be present in the impedance spectra, especially when dealing with porous interfaces. The equivalent impedance of a CPE is given by:

$$Z_{CPE} = \frac{1}{Q(j\omega)^\beta} \tag{3.7}$$

where Q is called CPE prefactor, β is the CPE index, j is the imaginary unit and ω is the small-signal angular frequency [104]. For what concerns the components denoted in lowercase letter

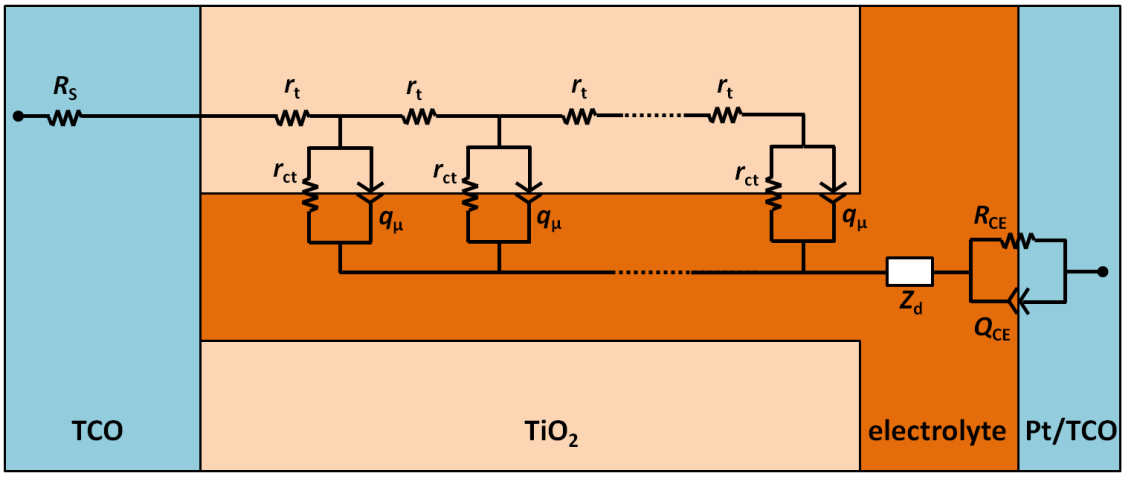

Figure 3.5: Simplified equivalent circuit of a DSC.

in the above list, which are r_t, r_{ct} and c_μ, they are considered as material properties that are independent on the photoanode thickness, because they are distributed in a repetitive arrangement of a transmission line (this is the reason for the Transmission Line Model name given to this circuit), with an equivalent impedance Z_{ph}. With the above reported considerations, by neglecting the electron recombination through the TCO substrate and the contact resistance between the TCO and the TiO_2 layer, and by replacing the ideal capacitors with the constant phase elements, the modeling circuit can be modified as reported in Fig. 3.5; the total cell impedance can be written as:

$$Z = R_S + Z_{ph} + Z_d + Z_{CE} \tag{3.8}$$

The components of this circuit (the series resistance, the photoanode impedance, the electrolyte impedance and the counter electrode impedance) will be described in the following.

Series resistance. The contribution of the series resistance is due to the sheet resistance of the substrates and also to the electrical wiring; this value is constant for each frequency, and also it does not change upon illumination and bias voltage.

Photoanode impedance. The impedance related to the oxide/electrolyte interface accounts for the so-called *diffusion-reaction model*, because it gives information about the electron transport properties of the semiconductor layer and about the recombination properties at the interface with the liquid solution (see Section 2.2.1). The general photoanode impedance has the form [108]:

$$Z_{ph} = \left[\frac{R_{ct}R_t}{1+(j\omega/\omega_n)^\beta}\right]^{1/2} coth\left\{(\omega_n/\omega_t)^{\beta/2}[1+(j\omega/\omega_n)^\beta]^{1/2}\right\} \tag{3.9}$$

where

$$\omega_t = \frac{1}{(r_t q_\mu d^2)^{1/\beta}} = \frac{1}{(R_t Q_\mu)^{1/\beta}} = \frac{1}{\tau_t} \tag{3.10}$$

is the *characteristic frequency of diffusion* in the semiconductor layer, and

$$\omega_n = \frac{1}{(r_{ct} q_\mu)^{1/\beta}} = \frac{1}{(R_{ct} Q_\mu)^{1/\beta}} = \frac{1}{\tau_n} \tag{3.11}$$

is the *rate constant for recombination* at the interface. As reported in Eqs. 3.10 and 3.11, both ω_t and ω_n are the inverse values of the most used parameters of transport time and lifetime, respectively. By fitting the experimental EIS curve using the circuit depicted in Fig. 3.5, the chemical diffusion coefficient can be evaluated by using the formula:

$$D_n = \omega_t \cdot d^2 = \frac{d^2}{(R_t Q_\mu)^{1/\beta}} = \frac{d^2}{\tau_t} \tag{3.12}$$

Starting from the Eq. 3.12, the diffusion length L_n can be evaluated by using Eq. 2.9. As stated in Section 2.2.1, in order to have an efficient electron collection L_n needs to be higher than the oxide thickness (or electron transport time lower than lifetime). By combining the Eqs. 2.9, 3.10, 3.11, and 3.12 the following relation can be found:

$$L_n = d \left(\frac{R_{ct}}{R_t} \right)^{\frac{1}{2\beta}} \tag{3.13}$$

Looking at Eq. 3.13, in order to have $L_n > d$, R_{ct} needs to be higher than R_t, i.e. the recombination resistance must be larger than transport resistance. In the opposite case, which is when large recombination occurs, only a fraction of the photogenerated carriers is collected and the condition $R_t >> R_{ct}$ applies; the general impedance of Eq. 3.9 becomes:

$$Z_G = \left[\frac{R_{ct} R_t}{1 + (j\omega/\omega_n)^\beta} \right]^{1/2} \tag{3.14}$$

known as *Gerisher impedance* [107]. This behavior corresponds to the diffusion in semi-infinite space, meaning that when transport resistance is large, the diffusion in the semiconductor becomes the limiting process in the device.

All the impedance elements related to the photoanode/electrolyte interface are strongly dependent on the distribution of CB electrons, and so their behavior depends on illumination and potential conditions. In particular the chemical capacitance, reflecting the density of states, is larger for high potential values but is quite independent from illumination. Regarding the transport resistance, its value remains constant as the light intensity varies for a given value of bias voltage; for this reason, the electron transport time (see Eq. 3.10) does not have an illumination dependency. On the other hand, while the applied potential is increasing, the TiO_2 Fermi level is displaced toward CB edge, thus increasing the free electron concentration and, as a consequence, the oxide conductivity. Accordingly, the transport resistance presents an exponential dependence on the bias voltage, becoming negligible for values around the open circuit voltage, because the oxide becomes sufficiently conductive. For potentials near V_{oc}, the circuit proposed in Fig. 3.5 can be reduced to the one in Fig. 3.6: the photoanode impedance can be modeled through the parallel $R_{ct}//Q_\mu$, in which the sum of the contributions of the distributed element components r_{ct} and q_μ is replaced by the concentrated element R_{ct} and Q_μ, respectively. For what concerns the recombination resistance, also its value exhibits the same exponential voltage dependency of R_t, but it also

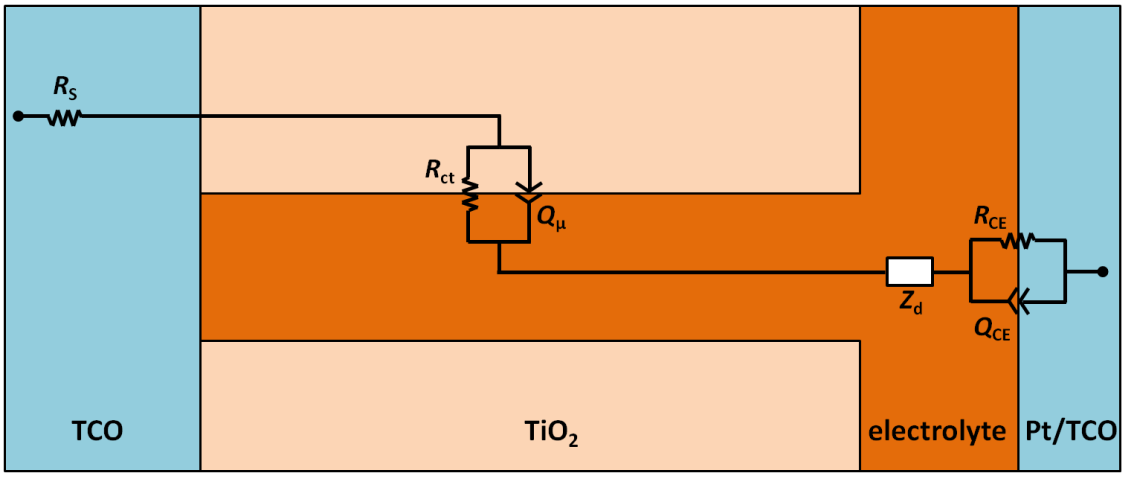

Figure 3.6: Simplified equivalent circuit of a DSC for TiO_2 in conductive state.

depends on the illumination conditions: for example, under dark its value is higher with respect to illumination, and correspondingly the dark electron lifetime is larger than under light. This can be explained with a difference of local I_3^- concentration (which is responsible for the electron recombination). In fact under illumination the I_3^- can be formed near the oxide/electrolyte interface because of the large number of oxidized dye molecules, while under dark it is formed at counter electrode and then it can diffuse towards the semiconductor. The higher concentration of holes produced in proximity of the TiO_2 can be responsible for the reduction of the electron lifetime [105].

Electrolyte impedance. As stated in Section 2.2.1 the charge transport in the electrolyte solution is a diffusion-driven process, which can be described by the so-called finite length Warburg impedance equal to [105, 106]:

$$Z_d = R_d \sqrt{\frac{\omega_d}{j\omega}} tanh\left(\sqrt{\frac{j\omega}{\omega_d}}\right) \tag{3.15}$$

in which R_d is the *electrolyte diffusion resistance*

$$R_d = \frac{k_B T \delta}{N^2 q^2 C_{I_3^-} D_{I_3^-}} \tag{3.16}$$

and ω_d is *characteristic frequency of diffusion* in the electrolyte solution:

$$\omega_d = \frac{D_{I_3^-}}{\delta^2} \tag{3.17}$$

Here N is the number of electrons transferred in the overall electrode reaction and $C_{I_3^-}$ is the steady state bulk concentration of I_3^- (usually I^- contributes little to the overall diffusion impedance which is mainly determined by the motion of I_3^-, because the concentration of triiodide is much lower than that of iodide and the latter diffuses faster than the former ion). The characteristic frequency ω_d depends on the diffusion coefficient $D_{I_3^-}$ and on the thickness of the diffusion layer δ (approximately equal to the half of the electrolyte layer thickness [63]).

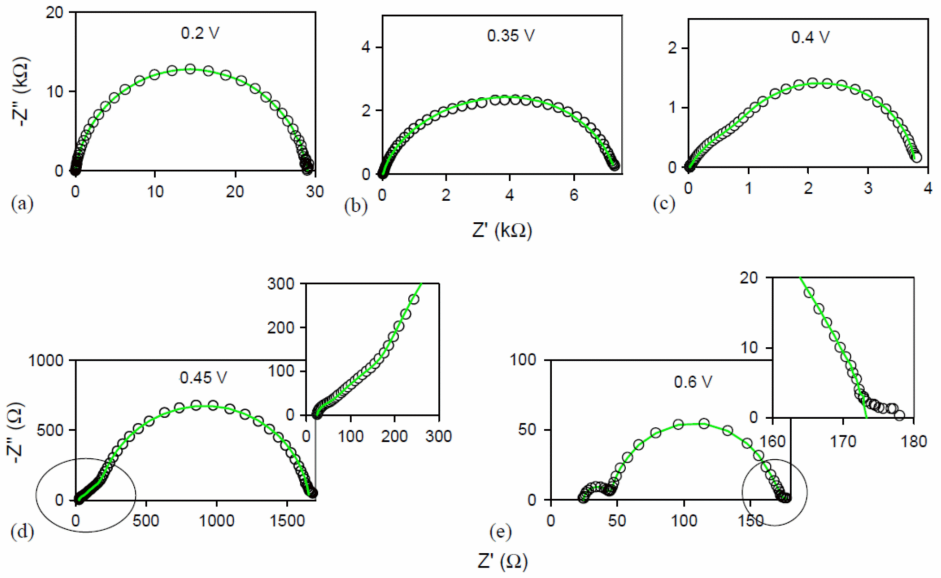

Figure 3.7: Impedance spectra of a DSC for different applied voltages. The point are experimental data, the lines are fit results. Insets represent the zoom of the area marked with the circle (adapted from [107]).

Counter electrode impedance. The counter electrode impedance accounts for the charge transfer at the Pt/electrolyte interface; its expression is given by [105]:

$$Z_{CE} = \frac{R_{CE}}{1 + j\omega(R_{CE}Q_{CE})^{1/\beta_{CE}}} = \frac{R_{CE}}{1 + j\omega\tau_{CE}} \tag{3.18}$$

where

$$\tau_{CE} = (R_{CE}Q_{CE})^{1/\beta_{CE}} \tag{3.19}$$

is the *counter electrode charge transfer time*. The value of the counter electrode impedance is practically non dependent on the applied bias voltage.

3.5.2 Impedance plot of a DSC

As introduced in Section 2.2.1, the charge transfer mechanisms into DSC are characterized by different time constants, so in the electrochemical impedance spectrum diverse features related to these processes can be observed [107]:

- the charge transfer at counter electrode (above 1 kHz);
- the electron transport in the TiO_2 layer (between 100 Hz and 1 kHz);
- the electron-hole recombination (between 1 and 100 Hz);
- the diffusion into the electrolyte (for frequencies lower than 1 Hz).

Typical impedance spectra of a DSC for different applied bias voltages are reported in Fig. 3.7. As explained in Section 3.5.1, the impedance elements in the equivalent circuit have different

behavior depending on the potential conditions: this is the reason for the strong variations that can be observed in the shape of the impedance plots.

Starting from low applied potentials (Fig. 3.7a), the characteristic curve is constituted by a single semicircle displaced from the origin by a quantity R_S (the contribution of the series resistance is in fact a displacement between the origin of axis and the curve intercept at high frequency). Since in this case the TiO_2 film can be considered as an insulator, the impedance related to substrate/oxide/electrolyte interface can be reduced to the parallel between the resistance R_{TCO} and the capacitance C_{TCO}, in series with the resistance R_S. At higher frequencies, a small deformation of this single arc occurs (but it is practically not visible due to overlap with the main arc), and this feature is attributed to the counter electrode impedance. Since for low applied voltages the currents flowing through the cell are very small, the I_3^- diffusion can be neglected, so no feature is observed in the low frequency regime.

For slightly higher potential values, the effect of the electrolyte diffusion starts to gain importance and a low-frequency feature begins to be visible (Fig. 3.7b).

Fig. 3.7c and Fig. 3.7d present the spectra for intermediate bias voltages: in these cases the full equivalent circuit (Fig. 3.5) has to be used in order to fit the experimental data. In particular the diffusion behavior in the oxide is clearly appreciable in the high frequency part, with a slope equal to $tan\left(\beta\frac{\pi}{4}\right)$ (the slope is close to 1 for ideal capacitance, see inset of Fig. 3.7d). In fact the Eq. 3.9 reduces to high frequency to the expression [108]:

$$Z = \sqrt{\frac{R_t}{Q_\mu}}(j\omega)^{-\beta/2} \tag{3.20}$$

For higher potential values, when the oxide moves towards a conductive state, the transport resistance becomes negligible and its contribution cannot any more be observed in the impedance spectra (in this case the circuit of Fig. 3.5 reduces to that reported in Fig. 3.6). The corresponding Nyquist plot is reported in Fig. 3.7e: the high-frequency semicircle is related to the parallel connection of R_{CE} and Q_{CE} from the counter electrode, the intermediate semicircle is the combination of R_{ct} and Q_μ , and the small feature at the lowest measured frequencies (inset of Fig. 3.7e), is the effect of I_3^- diffusion in the electrolyte.

Chapter 4

Experimental

In this chapter the materials and the instruments involved in this thesis work will be presented. Firstly the materials used for the microfluidic DSC fabrication and the device assembly procedures will be described, then the instruments exploited for the material and cell characterization will be introduced.

4.1 Materials and methods

Two different kinds of microfluidic DSC prototypes were designed and fabricated in this work. The first one had a rectangular geometry, the second a circular one. In the following they will be addressed as *type-I* cell and *type-II* cell, respectively. In Fig. 4.1 the two types of architecture are shown.

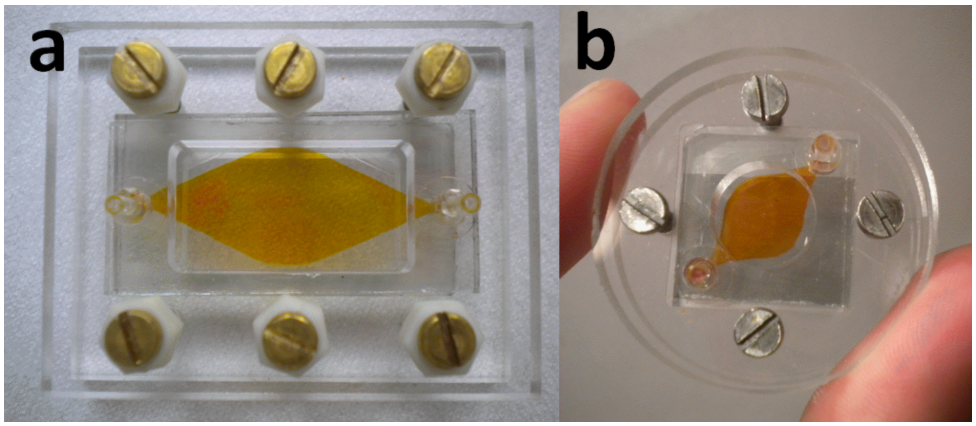

Figure 4.1: Photograph of the type-I (a) and type-II (b) microfluidic DSCs.

4.1.1 Photoanodes

In this paragraph the different materials and procedures used for the fabrication of the photoanodes will be described. For all the photoanodes, FTO-covered glasses (0.22 cm-thick, 7 Ω/sq, Solaronix) were used as transparent substrates. They were cut into 2 cm × 4 cm pieces for the type-I cell and into 2 cm × 2 cm pieces for the type-II. Before use, they were immersed in acetone in an ultrasonic bath for 10 min, then rinsed with ethanol and dried under nitrogen flow. The substrates were then cleaned for 10 min in a 3:1 (sulfuric acid:hydrogen peroxide) *piranha* solution in order to remove organic residues, abundantly rinsed with deionized (DI) water and dried with N_2 flow.

4.1.1.1 TiO_2 nanoparticles

The TiO_2 NPs were used as standard material for photoanodes.

The TiO_2 layer (Ti-Nanoxide D37 paste, Solaronix) was deposited onto FTO by tape casting technique; for type-I cell the chosen geometry was a square with sides of 6 mm, for type-II it was a circle with a diameter of 10 mm. After deposition, the layer was dried for 30 min at 50 °C on a hot plate (type-I) or dried for 10 min at 50 °C on a hot plate and then at room temperature for 30 min (type-II). Finally a sintering process at 450 °C for 30 min allowed the interconnection among the TiO_2 nanoparticle network, with a final film thickness of 7.5 ± 0.5 μm. The TiO_2 NP-based photoanode will be referred in the following as the *standard photoanode*.

In order to increase the photovoltaic performances of TiO_2 NP-based devices, some samples (see Section 6.4) were treated with $TiCl_4$. The expected effect of the treatment is a downward shift of the oxide CB that enhances the electron injection efficiency thus resulting in an increase of the short circuit current density [109]. For these samples, the sintered photoanodes were treated with $TiCl_4$ in a 50 mM aqueous solution for 20 min at 70 °C and then heat treated again at 450 °C.

In order to have a thicker porous oxide, for some cells (Section 6.5) a TiO_2 layer obtained combining Ti-Nanoxide D37 and D37/SP pastes (Solaronix) was deposited and sintered with the same procedure described above for type-II photoanode. In this case a film thickness of 16.0 ± 0.5 μm was obtained.

4.1.1.2 Sponge-like ZnO

A novel porous ZnO exploiting sponge-like morphology was successfully employed as DSC photoanode material.

Zinc nanostructured layers with different thicknesses (5, 8, 12.5 and 15 μm) were deposited by radio-frequency (RF) magnetron sputtering onto FTO-covered glass slices (type-II devices), using Ar plasma and pure (99.99%) Zn target. The geometry of the sputtered layer was circular with a diameter of 10 mm. Deposition conditions (gas flux, chamber pressure, and RF power) were optimized to control the nano-morphology of the film, and are reported in ref. [110]. After deposition, Zn films were thermally oxidized at 380 °C for 60 min in ambient condition.

4.1.1.3 TiO_2 nanotubes

TiO_2 nanotube (NT) membranes were also used as photoanode material.

TiO_2 NT arrays with different lengths (12, 22 and 30 μm) were fabricated by anodic oxidation of Ti foil in an electrolytic solution consisting of 0.5 wt% NH_4F and 2.5 vol% DI water in ethylene glycol, applying a constant voltage of 60 V for 2, 3 or 4 hours. Free-standing NT membranes were detached by the metal substrate and bonded on the FTO surface (type-II) employing a drop of TiO_2 sol prepared by sol-gel technique using titanium (IV) isopropoxide as precursor and Tween 20 as non-ionic surfactant (details about NT membrane fabrication and TiO_2 sol preparation are reported in ref. [111]). After bonding, the samples were left at room temperature overnight and then heat treated at 450 °C for 1 h for crystallization. Some samples (Section 6.4) were $TiCl_4$-treated following the procedure described above for NPs.

4.1.2 Sensitizers

4.1.2.1 Metal-organic dyes

N719 dye (Ruthenizer535bis-TBA, Solaronix) was chosen as standard sensitizer for device fabrication. Photoanodes were heated at 70 °C before impregnation, and then soaked in the sensitizing solution at room temperature. The standard solution was constituted by a fixed concentration of 0.2 mM of dye dissolved in ethanol, and the impregnation time was fixed at 24 h. After impregnation, the dyed photoanodes were rinsed in ethanol in order to remove the unabsorbed dye molecules.

For devices based on sponge-like ZnO photoanodes (Section 6.3), the concentration of dye in solution was fixed at 0.25 mM, and in some cases 0.2 mM of NaOH was added to the solution in order to increase its pH (thus moving its value from 6.5 to 9). Moreover different impregnation times were chosen, namely 10 min, 30 min, 1 h, 2 h, 5 h and 24 h.

For devices based on TiO_2 nanotube photoanodes (Section 6.4), the concentration of dye in solution was fixed at 0.3 mM, and the impregnation time was fixed at 18 h.

4.1.2.2 Organic dyes

Different organic dyes produced by Cyanine Technologies s.r.l. were tested, namely CT1, CT3, CT7, CTX1 and CT10 (see Section 6.2.1). For these tests, two different solutions were prepared for each sensitizer: the first one by dissolving 0.25 mM of dye in ethanol, the second one by dissolving 0.25 mM of dye in acetonitrile. For all the above described solutions the impregnation time was fixed at 24 h.

A detailed study was performed on hemi-squaraine dye (CT1). In this case (Section 6.2.2) the sensitizer solution was prepared by mixing 0.25 mM of dye in acetonitrile, and the impregnation time was fixed at 5 h. In some cases chenodeoxycholic acid was added to the solution (using two different concentrations, 1 mM and 10 mM) in order to reduce dye aggregation (see Section 2.1.3).

4.1.3 Counter electrodes

Pt was chosen as catalyst for the reduction reaction at cathode.

For counter electrode fabrication, the same transparent substrates used for the photoanode were employed. Two small pin-holes for electrolyte inlet/outlet were drilled in the FTO-covered glasses through powder blasting technology and then the substrates were cleaned with the same method described on Section 4.1.1. A thin layer of platinum (5 nm) was deposited on TCO by thermal evaporation. A 0.125 mm Pt wire (99.99% purity, Goodfellow) was put in a W crucible (ME5.005W, Testbourne) and connected with a high current circuit controlled by a variac. The evaporation current was in the range 90 – 110 A, as measured by a clamp meter. Deposition occurred in high vacuum conditions (pressure lower than $5 \cdot 10^{-7}$ mbar), which were obtained by means of a series of a mechanical and a turbomolecular pump. The distance between the metal source and the substrate was 10 cm. The thickness of the deposited layer was measured by a quartz crystal microbalance and the deposition rate was maintained constant at 0.01 nm/s.

In some cases, for the fabrication of non-fluidic DSC (see Section 5.3.2), non-drilled Pt-covered counter electrodes were used.

4.1.4 Electrolyte

The used electrolyte solution (Iodolyte AN 50, Solaronix) was based on iodide/triiodide redox couple dissolved in acetonitrile.

4.1.5 Housing system and cell assembly

Poly(methyl methacrylate) (PMMA) mechanical clamping system consisting in two identical frames with inlet/outlet ports was fabricated using a Benchman VMC4000 numerical control milling machine; the shape of the housing was rectangular (type-I) or circular (type-II). The same instrument was used for the fabrication of the masters for polydimethylsiloxane (PDMS) membrane casting (rectangular for type-I or circular for type-II) and O-ring interconnections.

The membranes were prepared by mixing PDMS pre-polymer and curing agent (Sylgard 184, Dow Corning) in a 10:1 weight ratio (for type-I) or 5:1 weight ratio (for type-II) and degassed at room temperature for 1 h. The mixture was then poured into the double-drop shaped mould and cured in a convection oven for 1 h at 70 °C. Finally the membrane was peeled off from the mould.

Cells were assembled by sandwiching the membrane between the dyed photoanode and the counter electrode, and closing the structure with the PMMA clamping through the use of screws. The strength applied to the screws was controlled by a torque spanner, in order to allow a good degree of reproducibility in the cell assembly. The electrolyte filling was done with a syringe connected to the housing ports (PDMS O-ring interconnections) via low-density polyethylene (LDPE) tubes. The ports were finally sealed employing homemade caps consisting in LDPE tubes obstructed with PDMS. For the non-destructive analysis on the cell components over time (see Section 6.5), the ports were left open during cell operation in order to induce an accelerated degradation of the components through spontaneous inlet of air and water vapor inside the mi-

crofluidic chamber. When non-drilled counter electrodes were used (Section 5.3.2), the filling was done by soaking up an electrolyte droplet between the electrodes and the cell closure was obtained by using two clips.

The external electrical contacts were obtained by depositing a silver paint (Elecolit 340) onto TCO layer (type-I architecture) or using copper foils (50 μm-thick, area 1.5 cm^2) for type-II.

4.2 Characterization

Field Emission Scanning Electron Microscopy (FESEM) was exploited for all the morphological characterizations performed in this work. The instrument used was a Zeiss SUPRA 40 equipped with a dedicated secondary electron detector (IN-LENS detector) and an annular solid state backscattered electron detector. The topography of the samples was investigated both in top view and in cross view (electron energy 5 keV). The morphological investigation was performed on Pt covered counter electrodes (see Section 6.5), on sponge-like ZnO nanostructures (see Section 6.3) and on TiO_2 nanotubes (see Section 6.4).

Both sponge-like ZnO nanostructure (see Section 6.3) and TiO_2 nanotube (see Section 6.4) crystalline structure was investigated by means of X-Ray Diffraction technique (XRD). A Panalytical PW1140-PW3020 diffractometer, equipped with a Cu K_α X-ray source, was used. In order to minimize the contribution of the substrate to the observed diffracted intensities, the scans were performed in a parallel beam geometry with a fixed angle of incidence equal to 1.5°.

Wettability of DSC counter electrodes (see Section 6.5) was studied by means of static Contact Angle (CA) measurement by using a DataPhysics OCAH 200 instrument in ambient atmosphere. The sessile drop method [112] was implemented employing a DI water droplet with 1 μL volume. Measurements were acquired in three different positions of each sample and the obtained CA value is the mean of the three measurements.

Profilometry measurements on all the TiO_2 NP-based photoanodes were performed by means of KLA-Tencor P.10 instrument in order to obtain the oxide layer thickness.

All the UV-visible spectroscopy measurements were carried out by means of a Varian Cary 5000 spectrophotometer equipped with an integrating sphere for diffuse and specular reflectance. In particular, transmittance measurements were performed on counter electrodes (see Section 6.5), while absorbance spectra of the photoanodes were acquired on N719 covered-TiO_2, (Section 6.5), CT1 covered-TiO_2 (Section 6.2.2) and N719 covered-ZnO (Section 6.3); in order to obtain the absorbance spectrum of the sensitizer attached to the oxide surface, the measurements were performed before and after the dye impregnation step. Furthermore the absorbance spectrum of CT1 dye in ACN solution was measured. For all the absorbance measurements, the Kubelka-Munk function

$$F(R) = \frac{(1-R)^2}{2R} = \frac{k}{s} = \frac{aC}{s} \tag{4.1}$$

(where R stands for the reflectance, k for the absorption coefficient, s for the scattering coefficient, C for the concentration of absorbing species and a for the absorbance) was evaluated, in order to

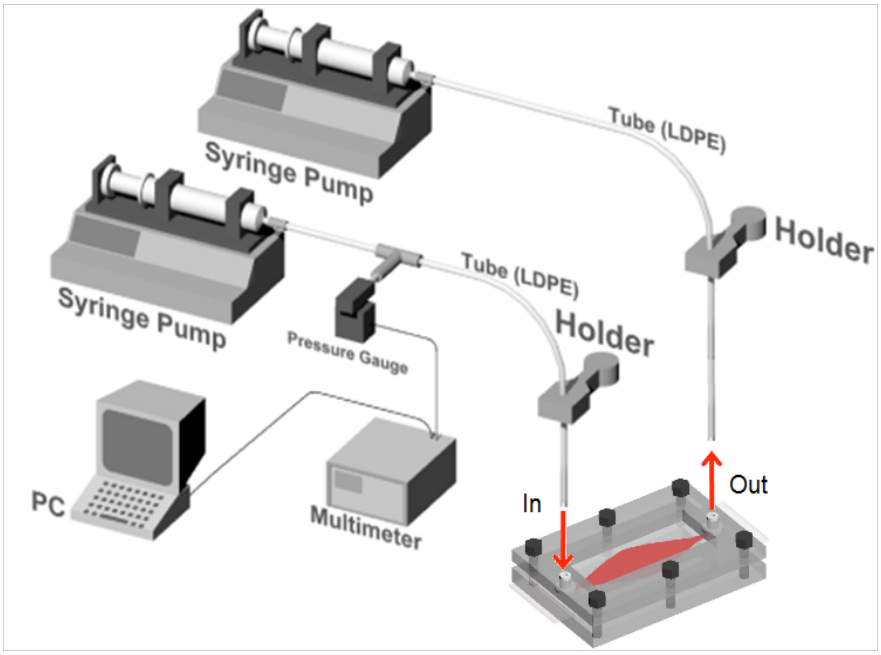

Figure 4.2: Experimental set-up exploited for the fluidic tests.

correlate reflectance and absorbance [113].

Sealing performances of the microfluidic architecture were studied by measuring the dynamic pressure endurance at different pressure values and at different temperatures. The fluidic characterization was carried out by means of a homemade set-up (see Fig. 4.2) consisting in a syringe pump (Harvard Apparatus 33) connected, through a 'T' joint, to a commercial pressure transducer (Honeywell 26PCFFA6G) and to the device PDMS interconnection via LDPE tubes. Pressure data as a function of time were recorded through a multimeter (Agilent Technology 34970A) interfaced to a PC. Measurements were performed by injecting the electrolyte solution at a fixed flow rate (50 μL/min) up to the maximum pressure value (25 and 50 kPa), followed by a 10 min steady state regime obtained by stopping the syringe pumping mechanism. The tests were conducted at two different temperatures: 50 and 80 °C. Subsequently, the microfluidic chamber was reinstated to the initial condition.

I-V electrical characterizations were carried out under AM1.5G illumination using a class A solar simulator (Newport 91195A) calibrated by means of a Si reference cell (VLSI SRC-1000-TC-QZ), and a Keithley 2440 SMU used to apply the bias voltages and to measure the photocurrent. The measurements for type-I devices were performed using a black mask with a hole that allowed illuminating the cells with an area of 0.16 cm^2, for type-II the illuminated area was 0.22 cm^2.

The IPCE spectra were acquired in DC mode using a Newport 100-W QTH lamp as light source and a 150-mm Czerny Turner monochromator (Lot-Oriel Omni-λ 150). The measured wavelength range was 300 – 800 nm with steps of 10 nm, and the current was measured by means of a Keithley 2440 SMU. The measurements for type-I devices were performed using a 0.16 cm^2 black mask, for type-II the mask area was 0.22 cm^2.

Open circuit voltage decay curves were measured using a CH Instruments 760D electrochemical workstation. The cells were initially kept under continuous 1 sun illumination using a solar simulator (Newport 91195A) until a constant photovoltage was reached, then the light was interrupted and the potential recorded as a function of the time with time-steps of 100 ms.

Electrochemical impedance spectra were collected through an electrochemical workstation (CH Instruments 760D) in the frequency range 10^{-1} – 10^{5} Hz with an amplitude of the sinusoidal signal of 10 mV. The cells were measured under illumination using a solar simulator (Newport 91195A) at open circuit voltage, and the experimental data were fitted by using the equivalent circuit of Fig. 3.6; the measurements for type-I cells were performed using a 0.16 cm^2 mask, for type-II the mask area was 0.22 cm^2. In some cases (see Section 5.5) the measurement were performed by varying the applied voltage (from 0 V to 0.8 V with 0.2 V step) both under illumination and in dark condition; moreover the cells based on TiO_2 nanotubes (see Section 6.4) were measured by varying the applied voltage between 0.5 V and 0.8 V only in dark condition. In both these two cases the experimental data were fitted exploiting the circuit depicted in Fig. 3.5.

Chapter 5

Microfluidic DSCs

5.1 Introduction

As already reported in previous sections (1.2.1 and 2.1.6), a critical fabrication step for DSCs is the electrolyte confinement and the related cell closure. The use of hot-melt sealants is generally adopted for closure and protection from the environment, but, for research purposes, this can be somewhat limiting. Indeed, some of the fabrication steps, as dye adsorption and electrolyte filling, are often performed without any active control, being difficult to ensure reproducibility and reliability while fabricating a large number of cells. Furthermore, both during experiments and after them, the cell, being irreversibly sealed, does not offer the possibility of control and inspection, or post-process modifications. In order to overcome this last problem, sometimes a simple assembling by using clips can be chosen, but in this cases the distance between the electrodes (and so the electrolyte volume) is not a fixed parameter, and again the fabrication reproducibility became hard to be obtained.

In this framework, a concrete aid could come from microfluidics. Microfluidics is the science and technology of systems that allow manipulating small amounts of fluids, using channels with dimensions in the micrometer scale range [114]. Its advantages lie in the ability to use very small amounts of reagents and to confine and carefully separate different liquids, allowing detection with high sensitivity and low amount of contamination. Moreover, a microfluidic structure can be interfaced with a housing system usually consisting of mechanical clamping, inlet/outlet ports and interconnections to external fluids handling devices. The use of low cost materials and technologies makes it appealing for versatile applications. In fact, the natural application scenario of microfluidics is in microbiology [115], but it has been shown to have a multidisciplinary approach that make it promising in a wide range of research fields, including energy conversion [116].

In this chapter the first application of microfluidic concepts in DSC fabrication is reported, in particular about the design of a housing test cell employing a polydimethylsiloxane thin membrane

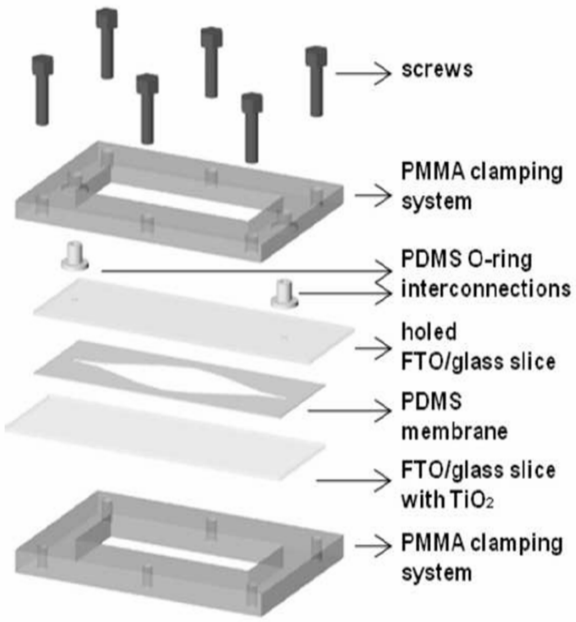

Figure 5.1: 3D sketch of type-I microfluidic-based DSC architecture.

reversibly sealed between the two electrodes by means of a poly(methyl methacrylate) clamping system. The proposed architecture was fully characterized in terms of sealing and photovoltaic performances. A slightly modified architecture (type-II structure) is then presented, which allows further reducing the amount of used materials and cell fabrication failures. The modified set-up electrical characteristics were evaluated and compared with the results reported in literature for irreversible sealed devices.

5.2 Type-I structure

In Fig. 5.1 a sketch of the type-I microfluidic DSC is reported. This structure is made up by all the elements that usually constitute a standard DSC, namely photoanode, electrolyte and counter electrode, but here the electrolyte solution is confined by means of a PDMS membrane. The complete housing consists on PMMA mechanical clamping, PDMS interconnections and the DSC itself, whose closure is guaranteed by the use of screws. A double-drop membrane layout was chosen to promote air bubble evacuation during electrolyte filling and a 50 μm retaining ring was designed near the chamber walls in order to improve the sealing at PDMS/FTO interfaces. The aid of PDMS press-fit interconnections with the integrated O-ring and the action of the clamping system avoided leakages during the electrolyte filling step. In Fig. 5.2 a photograph of the assembled device is presented, in which is possible to distinguish the dyed TiO_2 layer (the dark orange square) and the electrolyte solution contained in the microfluidic chamber.